HOKKAIDO UNIVERSITY

Title	Reintensification and Eyewall Formation in Strong Shear : A Case Study of Typhoon Noul (2015)
Author(s)	Shimada, Udai; Horinouchi, Takeshi
Citation	Monthly weather review, 146(9), 2799-2817 https://doi.org/10.1175/MWR-D-18-0035.1
Issue Date	2018-09
Doc URL	http://hdl.handle.net/2115/72852
Rights	
Type	article
File Information	mwr-d-18-0035.1.pdf

Instructions for use

Reintensification and Eyewall Formation in Strong Shear: A Case Study of Typhoon Noul (2015)

UDAI SHIMADA

Meteorological Research Institute, Tsukuba, Ibaraki, Japan

TAKESHI HORINOUCHI

Faculty of Environmental Earth Science, Hokkaido University, Sapporo, Hokkaido, Japan

ABSTRACT

Strong vertical wind shear produces asymmetries in the eyewall structure of a tropical cyclone (TC) and is generally a hostile environment for TC intensification. Typhoon Noul (2015), however, reintensified and formed a closed eyewall despite 200–850-hPa vertical shear in excess of $11 \, \mathrm{m \, s^{-1}}$. Noul's reintensification and eyewall formation in strong shear were examined by using Doppler radar and surface observations. The evolution of the azimuthal-mean structure showed that the tangential wind at 2-km altitude increased from 30 to $45 \, \mathrm{m \, s^{-1}}$ in only 5 h. During the first half of the reintensification, the azimuthal-mean inflow penetrated into the ~40-km radius, well inside the radius of maximum wind (RMW), at least below 4-km altitude, and reflectivity inside the RMW increased. As for the asymmetric evolution, vigorous convection, dominated by an azimuthal wavenumber-1 asymmetry, occurred in the downshear-left quadrant when shear started to increase and then moved upshear. A mesovortex formed inside the convective asymmetry on the upshear side. The direction of vortex tilt between the 1- and 5-km altitudes rotated cyclonically from the downshear-left to the upshear-right quadrant as the vortex was vertically aligned. In conjunction with the alignment, the amplitude of the wavenumber-1 convective asymmetry decreased and a closed eyewall formed. These features are consistent with the theory that a vortex can be vertically aligned through upshear precession. The analysis results suggest that the vortex tilt, vigorous convection, and subsequent intensification were triggered by the increase in shear in a convectively favorable environment.

1. Introduction

Tropical cyclones (TCs) form, intensify, and weaken in the presence of vertical wind shear, and shear is one of the most important factors accounting for changes in the structure and intensity of a TC. The interaction processes between a TC and shear, however, are very complicated and difficult to predict.

Vertical shear is known to be unfavorable for intensification. Statistically, intensifying TCs have weaker shear than nonintensifying TCs (Kaplan and DeMaria 2003). Further, shear predictors in statistical dynamical models have a weakening effect on intensity (DeMaria and Kaplan 1994, 1999; Knaff et al. 2005; DeMaria 2009; Kaplan et al. 2010). Paterson et al. (2005) and Wang et al. (2015) showed statistically that a 200–850-hPa wind shear of greater than ~$10 \, \mathrm{m \, s^{-1}}$ contributes to such

weakening. Explanations for the negative influence of shear on intensity include the following: (i) ventilation of the TC warm core and high potential vorticity (PV) by a relatively strong upper-level environmental wind (Frank and Ritchie 2001); (ii) strong downdrafts bringing midlevel low equivalent potential temperature (θ_e) air into the boundary layer, leading to a decrease in TC intensity from the perspective of a Carnot cycle heat engine (Riemer et al. 2010); and (iii) intrusion of midlevel dry air into the eyewall (Tang and Emanuel 2010). In addition, the effect of shear on intensity change is dependent not only on the shear magnitude, but also on vortex strength: stronger vortices are more resilient to shear (DeMaria 1996; Riemer et al. 2013; Rios-Berrios and Torn 2017).

Jones (1995) and Reasor et al. (2004) theorized that TC vortices have intrinsic resiliency against shear that keeps them vertically aligned. A tilted PV column can be decomposed into azimuthal-mean and wavenumber-1

Corresponding author: Udai Shimada, ushimada@mri-jma.go.jp

components (Reasor and Montgomery 2001). When the scale of the vortex is much smaller than the Rossby radius of deformation, the wavenumber-1 asymmetry behaves like a vortex Rossby wave (VRW) called a tilt mode (Reasor et al. 2004), which is similar to an edge wave on a Rankine vortex (Lamb 1932). The vortex precesses as the VRW propagates (Jones 1995) and is vertically aligned by the resonant damping of the tilt mode, provided that the sign of the radial gradient of PV at the critical radius, where the phase speed of the VRW and tangential wind speed are the same, is negative (Schecter et al. 2002; Schecter and Montgomery 2003). In this case, the vortex reaches an equilibrium tilt[1] of 90° to the left of shear (Reasor et al. 2004). In contrast, the vortex shears apart when the gradient at the critical radius is positive (Schecter et al. 2002). Meanwhile, when the PV gradient is 0 at the critical radius, the vortex undergoes repetitive cycles of tilting downshear, cyclonic precession upshear, and realignment (Reasor et al. 2004; Reasor and Montgomery 2015). Reasor et al. (2013) showed through a composite analysis of observations that TC vortices tend to be tilted downshear and to the left of the shear vector.

Previous studies have shown that maximum upward motion occurs in the downtilt direction, rather than in the downshear direction (Rogers et al. 2003; Zhu et al. 2004; Wu et al. 2006; Braun et al. 2006; Braun and Wu 2007; Ueno 2008; Riemer et al. 2010; Reasor and Eastin 2012; Reasor et al. 2013), and mechanisms have been proposed for this vertical motion asymmetry. When a vortex is tilted by shear, adiabatic upward (downward) motion is induced downtilt (uptilt) as a transient response to maintain thermal wind balance in the tilted vortex, and this response causes a negative (positive) temperature anomaly downtilt (uptilt) (Jones 1995; Wang and Holland 1996; Frank and Ritchie 1999; Ueno 2007). Following this response, diabatic processes allow a balance to be established between horizontal advection of vorticity by low-level storm-relative inflow (outflow) and vortex stretching (shrinking) on the low-level inflow (outflow) side (Bender 1997; Frank and Ritchie 1999, 2001).

Through the mechanisms described above, vertical shear induces TC precipitation and convection structure with wavenumber-1 asymmetry (e.g., Black et al. 2002; Corbosiero and Molinari 2002, 2003; Corbosiero et al. 2006; Chen et al. 2006). Observation-based composite studies (Reasor et al. 2013; DeHart et al. 2014) have shown that for hurricane-strength TCs, eyewall convection is initiated by low-level deep inflow in the downshear-right quadrant. Intense updrafts grow hydrometeors downshear, causing radar reflectivity to be highest in the downshear-left quadrant. Downdrafts, which are associated with small-scale deep convection downshear left, dominate the upper levels of the upshear-left quadrant. Eyewall convection on the upshear side is suppressed by upper-level inflow and low-level outflow.

Some studies, however, have shown that moderate and strong shear[2] can contribute to intensification through the occurrence of vigorous deep convection, called convective bursts, inside the radius of maximum wind (RMW) on the downshear side (Molinari et al. 2006; Reasor et al. 2009; Molinari and Vollaro 2010; Nguyen and Molinari 2012). Molinari and Vollaro (2010) examined the intensification (a pressure fall of 22 hPa in less than 3 h) of Tropical Storm Gabrielle (2001) in the presence of a shear of $13\,\mathrm{m\,s^{-1}}$, and Nguyen and Molinari (2012) examined the intensification (an increase in the maximum 1-min sustained wind speed from ~ 33.4 to $48.9\,\mathrm{m\,s^{-1}}$ in 18 h) of Hurricane Irene (1999) in an environment of increasing shear, from 6–7 to $10–13\,\mathrm{m\,s^{-1}}$. Both Molinari and Vollaro (2010) and Nguyen and Molinari (2012) discussed that these storms were highly asymmetric, but that it was the projection of the asymmetric heating onto the axisymmetric component that was critical for intensification, based on the theoretical studies of Nolan and Grasso (2003), and Nolan et al. (2007). Meanwhile, Reasor et al. (2009) showed that Hurricane Guillermo (1997) intensified rapidly with asymmetric strong convection in the downshear-left quadrant under a shear of $\sim 7–8\,\mathrm{m\,s^{-1}}$ and emphasized the nonnegligible contribution of eddy momentum fluxes.

Even under the same moderate-shear environment, both intensifying and nonintensifying TCs are observed. Rogers et al. (2016) examined structural changes of Hurricane Edouard (2014) and showed that Edouard had deep vigorous convection in the upshear-left quadrant during intensification but little deep convection there during its maturity. Rios-Berrios and Torn (2017) demonstrated, through a composite analysis of intensifying and nonintensifying TCs under moderate shear conditions, that midlevel relative humidity and surface latent heat fluxes were larger in intensifying TCs, in particular, on the upshear side, than in nonintensifying TCs. We lack sufficient knowledge,

---

[1] Tilt is defined as the difference between the upper- and the lower-level vortex center locations.

[2] Here, we use three categories of 200–850-hPa shear based on the 25th and 75th percentiles of shear magnitude distributions around TCs (Rios-Berrios and Torn 2017): weak, $<4.5\,\mathrm{m\,s^{-1}}$; moderate, $4.5–11.0\,\mathrm{m\,s^{-1}}$; and strong, $>11.0\,\mathrm{m\,s^{-1}}$.
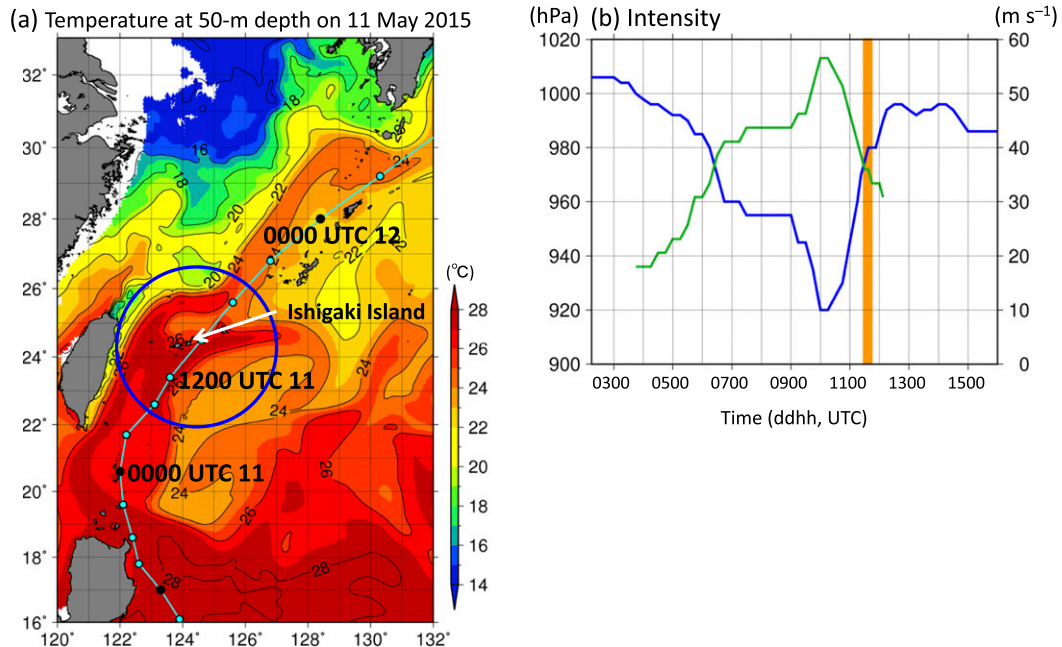
FIG. 1. (a) Ocean temperatures at 50-m depth (color scale) on 11 May 2015 and Noul's track. Light blue dots show the center location at 6-h intervals until 0600 UTC 11 May and at 3-h intervals after that time. Black dots show the center location at 1-day intervals (0000 UTC). The large dark blue circle centered at Ishigaki Island denotes the range of the Ishigaki Doppler radar, ∼200 km. The ocean temperature data were provided by the JMA. (b) Time evolution of Noul's intensity: maximum wind (green line) and central pressure (blue line). RSMC Tokyo's best track data do not include maximum wind speeds for a TC categorized as a tropical depression. The vertical orange bar indicates the period focused on in this study (1000–1800 UTC 11 May 2015).

however, of the causes of inner-core structure and intensity differences in actual TCs under moderate–strong shear conditions. One reason may be insufficient observational studies: because these processes occur over the ocean on a short time scale, even aircraft reconnaissance cannot necessarily observe them at the appropriate time.

Typhoon Noul (2015) appeared to reintensify as it passed near Ishigaki Island, Okinawa, Japan, from 1200 to 1800 UTC 11 May 2015 (Fig. 1a). Although this reintensification was not captured in the best track data of the Regional Specialized Meteorological Center (RSMC) Tokyo (Fig. 1b), vigorous convection occurred, and then the eyewall structure changed from asymmetric to symmetric in the presence of shear greater than $11 \, \mathrm{m \, s^{-1}}$. We present evidence for this reintensification in section 3a.

Why did Noul reintensify and acquire a closed eyewall structure despite strong shear? We use high-temporal-resolution surface observations and Japan Meteorological Agency (JMA) operational Doppler radar data to address this question. We aim to document the evolution of the inner-core structure of Noul, and to examine the processes involved in Noul's reintensification and the formation of a closed eyewall in a strong-shear environment.

We describe the data and the methods used in section 2. In section 3, we present an overview of Noul and associated environmental conditions. In section 4, we document the axisymmetric structure of Noul. In sections 5 and 6, we show the evolution of convective-scale structures and vortex tilt. We discuss features associated with Noul's reintensification in section 7. Section 8 presents the conclusions.

2. Data, methods, and accuracy evaluation

Data used in this study consisted of surface observations provided by the JMA, C-band operational Doppler radar data observed at Ishigaki Island (Fig. 1a), radar composite rainfall data provided by the JMA, infrared (IR) brightness temperatures (at $10.4 \, \mu\mathrm{m}$) from the *Himawari-8* geostationary satellite, and Japanese 55-year Reanalysis (JRA-55) atmospheric data (Kobayashi et al. 2015). The surface observations included maximum gust wind, temperature, dewpoint temperature (or relative humidity), precipitation, station pressure, and sea level pressure (SLP). Here, the maximum gust wind is the maximum 3-s mean wind speed and direction observed during each 1-min period. Equivalent potential temperature θ_e was calculated by using the formula
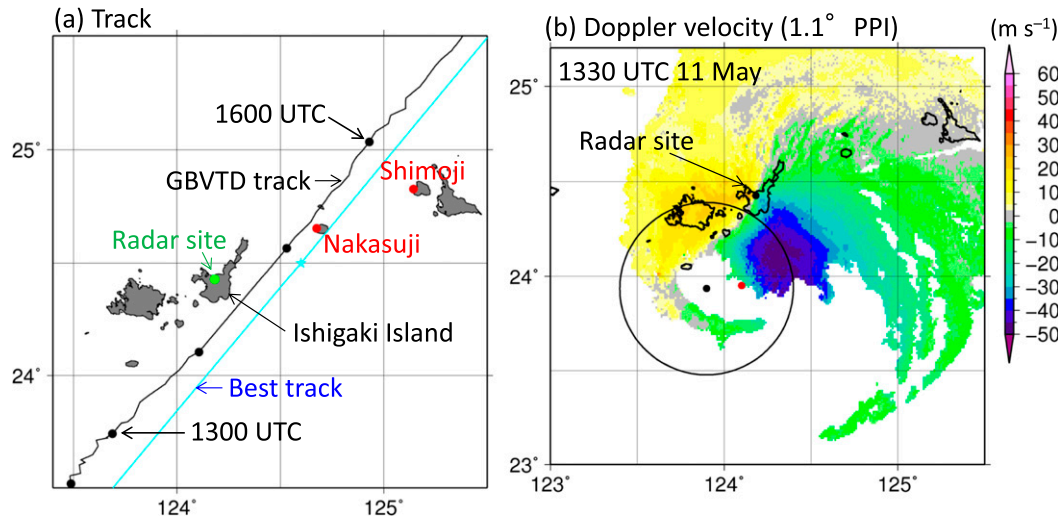
FIG. 2. (a) Noul's track. The black line shows the track obtained by the GBVTD-simplex method at 5-min intervals; the black dots are at 1-h intervals. The light blue line shows RSMC Tokyo's best track, and the light blue dot is the storm position at 1500 UTC 11 May. (b) Doppler velocity plan position indicator (PPI) pattern at a 1.1° elevation angle at 1330 UTC 11 May. The black dot indicates the center detected in this study, the red dot indicates the center location in RSMC Tokyo's best track data, and the black circle denotes the 1-km RMW.

of Bolton (1980). The Doppler observation parameters of the JMA radars have been reported by Shimada et al. (2016, their Table 1).

By applying the ground-based velocity track display (GBVTD) technique (Lee et al. 1999) to Doppler velocity, V_D, data, we retrieved the two-dimensional horizontal wind field at 1-km altitude intervals from 1 to 10 km of altitude for Noul. No boundary layer flow was retrieved because of the lack of V_D data. The dataset includes tangential winds with wavenumbers 0, 1, 2, and 3, and radial winds with wavenumbers 0 and 1 in storm-centered cylindrical coordinates. Details of the GBVTD-derived wind dataset are given by Shimada et al. (2018). The analysis period was from 1200 to 1700 UTC 11 May 2015. The GBVTD technique can retrieve the wind field only within the range of radii between the storm center and the radar location. Because no V_D observations could be made in the eye region, no winds were retrieved while the eye was over the radar site from 1405 to 1450 UTC 11 May.

In the GBVTD technique, the storm center is defined as the location that maximizes the axisymmetric tangential wind $\bar{v}$ on the scale of the RMW. To detect the storm center, we used the GBVTD-simplex center-finding method (Lee and Marks 2000; Bell and Lee 2012), in which the time continuity of the RMW, maximum $\bar{v}$, and the center location is used to find the center among candidate locations (for more details, see Bell and Lee 2012). As the likely scale of the RMW, the range of radii from 30 to 60 km was set in the simplex method. The RMW scale was not sufficiently covered in

the retrieval area, however, when the TC was within 60 km of the radar site. This condition introduced some uncertainty into the center-finding method and the resulting uncertainty of center locations is a limitation of this study. The storm center, defined as the center detected at 1-km altitude, was used in the GBVTD analysis to retrieve the axisymmetric component of the wind field at all altitudes. During the period of the wind dataset gap, the center locations were obtained by temporal interpolation. To examine the vertical tilt of Noul, we also detected the storm center at 5-km altitude, using the same method that we used at 1-km altitude. Centers above 5-km altitude could not be reliably detected because the Doppler velocity data were too sparse to obtain reasonable results.

Noul's track, as detected by the GBVTD-simplex method, was displaced a few tens of kilometers westward from RSMC Tokyo's best track (Fig. 2a). At 1330 UTC 11 May, as the TC approached the radar site on Ishigaki Island, the detected center location was in the middle of the newly formed eyewall and in an appropriate location for the V_D pattern. In contrast, the best track center location, obtained by interpolation of the best track data, was located near the eyewall where V_D was ~20 m s^{-1} (Fig. 2b). We consider that this result justifies our use of the detected track in this study.

As the metric to evaluate the quality of the wind data retrieved by the GBVTD technique, we used the overall average of the root-mean-square difference (RMSD) between the V_D resampled from the GBVTD-retrieved winds and the observed V_D. The RMSDs, which generally
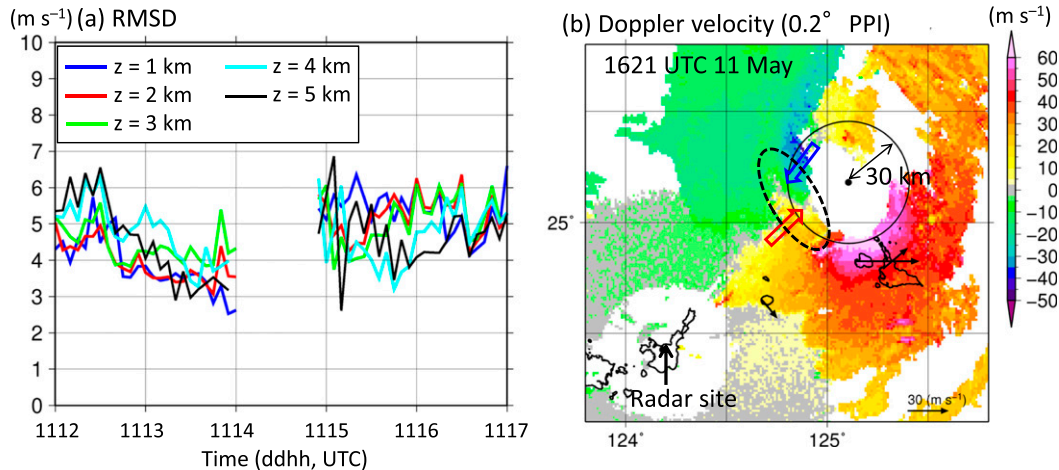
FIG. 3. (a) Time evolutions of the overall average RMSD between V_D resampled from the GBVTD-retrieved winds at altitudes from 1 to 5 km and observed V_D at altitudes from 1 to 5 km. (b) Doppler velocity PPI pattern at a 0.2° elevation angle at 1621 UTC 11 May. The black circle denotes a radius of 30 km as representative of the 1-km RMW. The small black arrows show gust wind vectors observed at around 1621 UTC, the bold red and blue arrows highlight the V_D directions, and the dashed ellipse marks a convergence area in the V_D field.

ranged from 3 to $6 \, \mathrm{m \, s^{-1}}$ (Fig. 3a), were larger values than those obtained by other case studies (Zhao et al. 2012; Shimada et al. 2018). The relatively poor quality of the GBVTD-retrieved winds is likely to stem from sparse radar coverage in the first half of the analysis period (e.g., Fig. 2b), noise contamination due to V_D aliasing (e.g., Fig. 3b), and the poor accuracy of the TC center-finding method (e.g., Lee and Marks 2000; Harasti et al. 2004; Bell and Lee 2012; Murillo et al. 2011). The distortion of the dipole V_D pattern associated with the inbound and outbound Doppler velocities (Fig. 3b), caused by the complicated flow, can also reduce the accuracy of the GBVTD-retrieved winds. Thus, the GBVTD-retrieved wind speeds have some uncertainty. For this reason, we did not use GBVTD-retrieved asymmetric wind data in this study; instead, we used maximum gust wind data observed at weather stations.

3. Overview of Typhoon Noul

a. Storm history and intensity

According to the best track data of RSMC Tokyo (Fig. 1), Typhoon Noul attained a lifetime minimum central pressure of 920 hPa at 0000 UTC 10 May 2015 over the Philippine Sea. Then, after passing just northeast of Luzon Island, it weakened rapidly. Noul was transformed into an extratropical cyclone at 0300 UTC 12 May. For more details of Noul, see the 2015 annual report of the JMA (2016).

In this study, we focus on the period beginning at 1000 UTC 11 May, a few hours before the central pressure in the best track data temporarily stopped increasing, and ending at 1800 UTC 11 May, a few hours before the central pressure started to increase again (Fig. 1b). At 1000 UTC 11 May, convective bursts occurred to the north (downshear-left quadrant) of Noul (Figs. 4a,b). After Noul passed near Ishigaki Island, the coldest IR brightness temperature was observed on the upshear-left side, but there was no well-defined eye (Fig. 4c).

Following the convective bursts, GBVTD-retrieved $\bar{v}$ at altitudes of 1 and 2 km increased rapidly from ~30 to ~45 $\mathrm{m \, s^{-1}}$ during only 5 h from 1200 to 1700 UTC 11 May (Fig. 5). This increase in $\bar{v}$ is evidence of Noul's reintensification. After 1545 UTC, $\bar{v}$ was almost the same at 1- and 2-km altitudes because the number of plan position indicator (PPI) scans from the Ishigaki radar was limited when Noul was far from the radar site, with the result that the constant-altitude plan position indicator (CAPPI) data, which were used in the GBVTD analysis, were almost the same at 1- and 2-km altitudes.

b. Environmental conditions

Around the onset of reintensification (1200 UTC), Noul was passing over the ocean south of Ishigaki Island, where temperatures at 50-m depth were greater than 27°C (Fig. 1a); then, after Noul passed near Ishigaki Island, ocean temperatures at 50-m depth along the track decreased to below 25°C.

Noul was under a westerly shear of ~11 $\mathrm{m \, s^{-1}}$ around the onset of reintensification, but by 1800 UTC the shear had increased to more than 16 $\mathrm{m \, s^{-1}}$ (Fig. 6). The forward speed of Noul was very fast; after 1300 UTC, it was
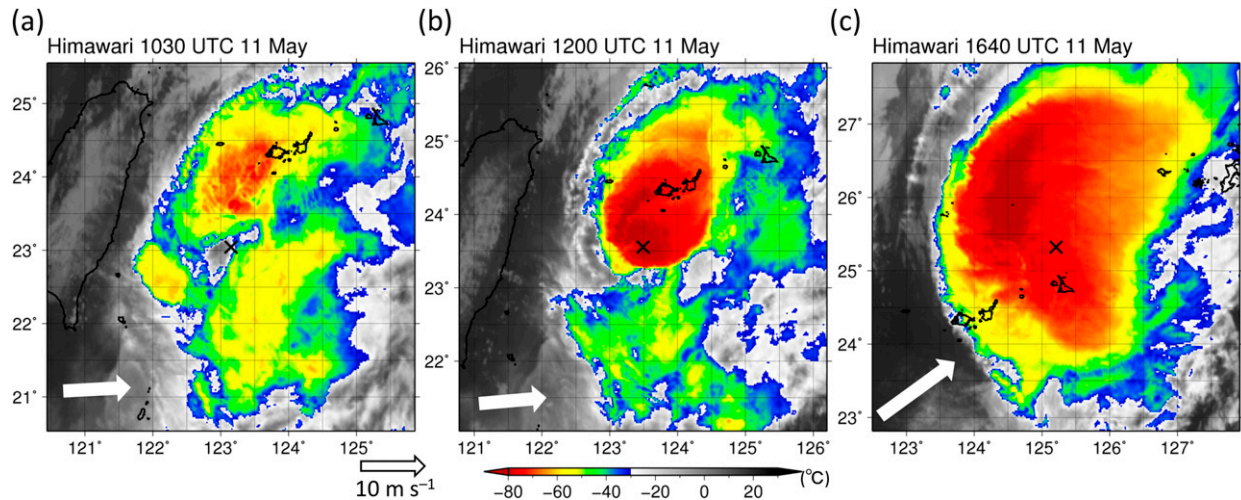
FIG. 4. Infrared brightness temperatures (at 10.4 μm) from the *Himawari-8* geostationary satellite at (a) 1030, (b) 1200, and (c) 1640 UTC 11 May. The $\times$ mark at the center of each panel indicates the approximate center of Noul, which was subjectively determined from radar imagery. The white arrow shows the 850–200-hPa shear vector.

greater than $10\,\mathrm{m\,s^{-1}}$, and after 1700 UTC it exceeded $20\,\mathrm{m\,s^{-1}}$. The gradual increases in shear and forward speed were caused by the influence of an upper-level jet associated with a deep trough over mainland China (not shown; discussed further in section 7b).

4. Axisymmetric structure

The axisymmetric structure of Noul changed dramatically during the 5 h (1200–1700 UTC 11 May) of the radar analysis. Hereafter, 1200–1400 UTC 11 May, before the gap in the wind dataset, is defined as period I of the analysis, and 1500–1700 UTC, after the gap, is defined as period II.

During period I, the axisymmetric structure of Noul at 1-km altitude shows that isopleths of the azimuthal-mean absolute angular momentum, $\overline{M} \equiv (1/2)fr^2 + r\overline{v}$, where f is the Coriolis parameter and r is radius, moved inward with time as the radial gradient of $\overline{M}$ increased (Fig. 7a); this result indicates that both $\overline{v}$ and absolute vorticity, $\zeta_a \equiv (1/r)(\partial \overline{M}/\partial r)$, increased. In addition, the RMW at 1-km altitude contracted from ~65 km at 1200 UTC to ~40 km by 1510 UTC (Fig. 7a). The vortex itself, however, was still weak and Noul did not yet have a well-organized eyewall. The $30\,\mathrm{m\,s^{-1}}$ contour of $\overline{v}$ and the 10-dBZ contour of radar reflectivity were at low altitudes and had wide radial widths (Fig. 8a). Below 4-km altitude, the inflow penetrated into a radius of 40 km, well inside the RMW (Figs. 7b and 8b), and outside the RMW the inflow at 1-km altitude exceeded $-4\,\mathrm{m\,s^{-1}}$ (Fig. 7b). From 1315 to 1430 UTC, azimuthal-mean reflectivity increased, and the radius of maximum reflectivity (RMR) was inside the RMW (Fig. 7c). The

increase in reflectivity inside the RMW and the low-level inflow in the vicinity of the RMW are generally favorable conditions for an increase in maximum $\overline{v}$ (Shapiro and Willoughby 1982; Pendergrass and Willoughby 2009; Nolan et al. 2007; Smith et al. 2009; Rogers et al. 2013; Smith and Montgomery 2016).

The accuracy of the GBVTD-retrieved winds appears poorer during period II than period I because the distributions of both $\overline{v}$ and $\overline{u}$ during period II were noisy (Figs. 7a,b); $\overline{v}$ fluctuated erratically, and inflow and outflow were mixed from 1530 to 1630 UTC (Fig. 7b). The 1-km RMW was sometimes within 20–25 km of the center, where the retrieved $\overline{v}$ was anomalously large (Fig. 7a).
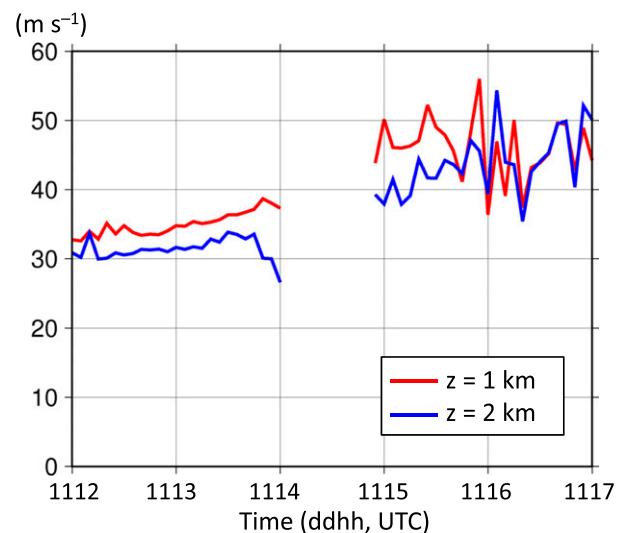

FIG. 5. Time evolutions of maximum azimuthal-mean tangential wind speed at altitudes of 1 and 2 km.
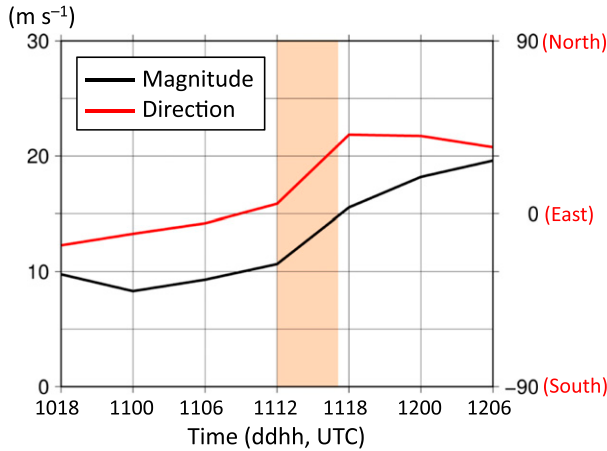
FIG. 6. Vertical wind shear (black line) and its heading direction (red line) between 200 and 850 hPa averaged within 500 km from the storm center. The shear was calculated from JRA-55 data (Kobayashi et al. 2015). The shaded bar indicates the radar observation period.

In spite of the uncertainty in $\overline{v}$ at 1-km altitude, $\overline{v}$ definitely increased until at least 1600 UTC. During period II, the $30\,\mathrm{m\,s^{-1}}$ contour of $\overline{v}$ and the 10-dBZ contour of reflectivity reached, on average, an altitude of 6 and 10 km, respectively (Figs. 8c,d). Azimuthal-mean reflectivity increased outside the RMW after 1500 UTC, and the 20-dBZ contour outside the RMR moved outward with time (Fig. 7c).

5. Convective-scale structure

a. Convective bursts

Noul's reintensification began with convective bursts. The rainfall imagery shows that, around the onset of reintensification (1200 UTC), intense convection was located downshear left, ~75 km from the storm center (Fig. 9a). This convection approached the storm center, playing a role in the contraction of the RMW (Figs. 9b,c), and moved cyclonically around the storm center from the downshear to the upshear side as it became organized into an eyewall (Figs. 9d,e). The convection weakened, but did not dissipate when it moved to the upshear side of the eyewall, where downward motion generally dominates the lower troposphere of TCs in shear (Reasor et al. 2013; DeHart et al. 2014). When the convection was active primarily inside the 5-km RMW, from 1315 to 1600 UTC (Figs. 9b,c,d), $\overline{v}$ increased rapidly at the 1- and 2-km altitudes (Fig. 5). Finally, by 1800 UTC, a closed eyewall had formed (Fig. 9f).

What caused the convective bursts? Sonde observations at Ishigaki Island, which was located in the downshear-left quadrants of Noul until ~1200 UTC 11 May, showed that the θ_e averaged over the lowest 500 m greatly exceeded the saturation equivalent potential temperature, θ_{es}, at altitudes from 2 to 10 km at 0600 UTC before the start of the convective bursts (Fig. 10). This sonde profile indicates the potential for
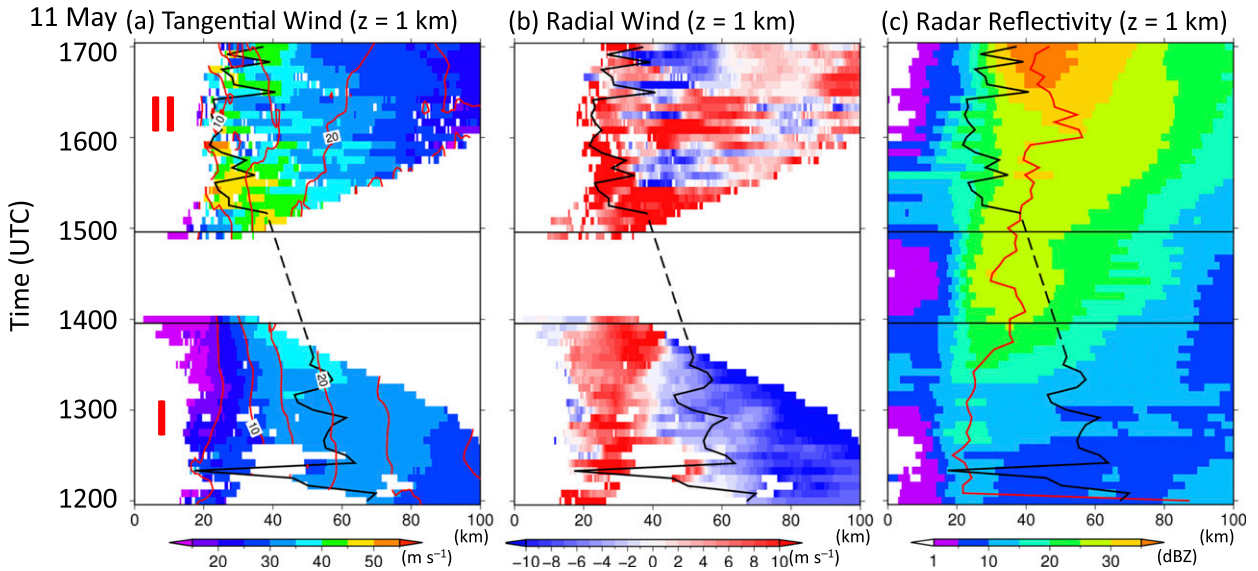

FIG. 7. (a) Radius–time Hovmöller diagram of $\overline{v}$ at 1-km altitude (color scale), $\overline{M}$ ($10^5\,\mathrm{m^2\,s^{-1}}$, purple contours), and RMW (thick black line). The blank areas are where the GBVTD technique could not retrieve $\overline{v}$ (i.e., during the TC's passage near Ishigaki Island). (b) Radius–time Hovmöller diagram of azimuthal mean radial wind $\overline{u}$ at 1-km altitude (color scale) and RMW at 1-km altitude (thick black line). The blank areas are where the GBVTD technique could not retrieve $\overline{u}$. (c) Radius–time Hovmöller diagram of azimuthal mean radar reflectivity at 1-km altitude (color), radius of maximum reflectivity (RMR; red line), and RMW (thick black line). The black horizontal lines indicate the period I and II boundaries.
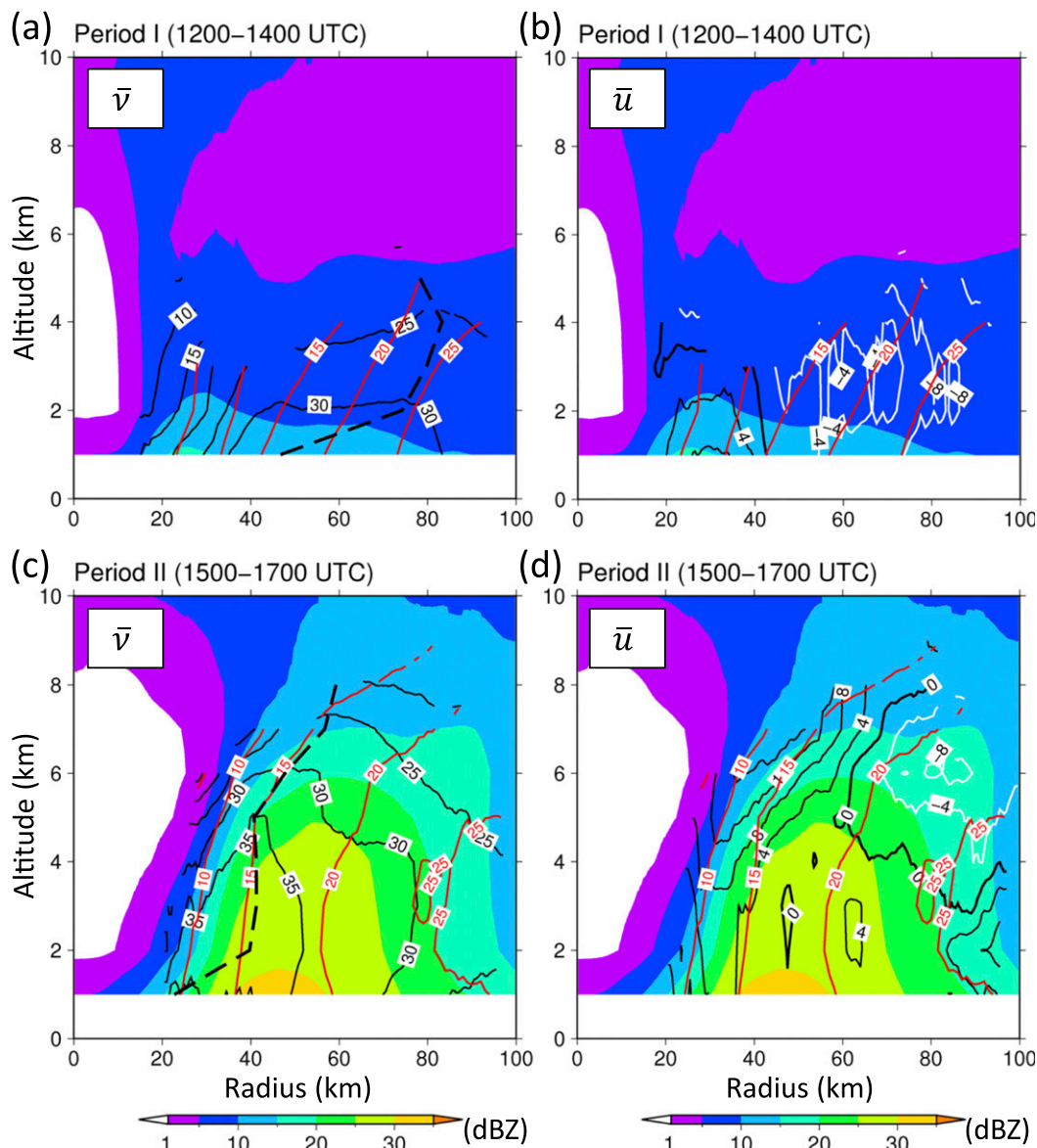
FIG. 8. Radius–height plots of (a) time-averaged $\bar{v}$ (m s^{-1}, black contours), azimuthal-mean radar reflectivity (color scale), and $\bar{M}$ (10^5 m^2 s^{-1}, red contours); and (b) time-averaged $\bar{u}$ (m s^{-1}, black contours positive, white contours negative), azimuthal-mean radar reflectivity (color scale), and $\bar{M}$ (10^5 m^2 s^{-1}, red contours) during period I. The dashed line is the RMW. Contours were drawn only in areas where there were observations averaged over at least 1 h in total. (c),(d) As in (a),(b), but for period II.

upright buoyant convection. Because storm-relative radial winds at the surface in the downshear-left quadrant were inflow (see section 5b), the convective bursts likely occurred in a convectively favorable environment.

b. Mesovortex

In association with the convective bursts, a mesovortex formed in the eye. To visualize the mesovortex, we plotted storm-relative (SR) surface winds at 4-min intervals at weather station locations relative to the

storm center at four specific times (e.g., plot periods A–D) (Fig. 11, Table 1). The SR winds were derived from surface gust wind observations.

During plot periods A–D, inflow was occurring on the downshear side and outflow on the upshear side of the storm. This radial flow pattern is generally observed in the lower troposphere of TCs in shear (e.g., Braun et al. 2006; Reasor et al. 2013). During plot period A (Fig. 11a), SR wind speed was ~30 m s^{-1} around 20 km northwest of the storm center inside the eyewall. During
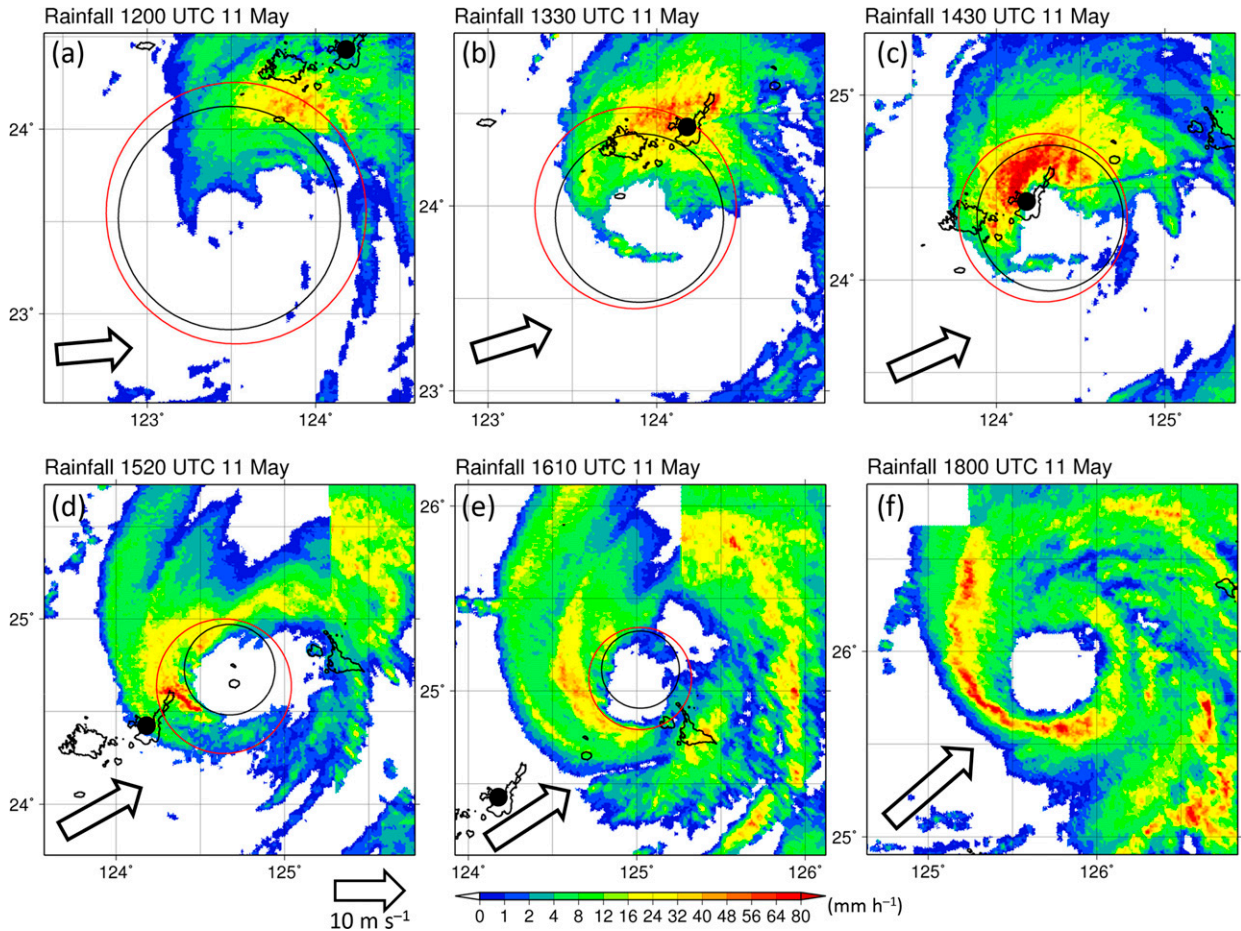
FIG. 9. (a)–(f) Radar composite rainfall rate (data provided by the JMA). In each panel, the bold black arrow shows the 850–200-hPa shear vector; the black dot indicates the radar site, and the black (red) circle denotes the 1-km (5 km) RMW. The 5-km RMW was obtained by using the 5-km centers in the GBVTD analysis. The center locations at 1- and 5-km altitudes in (c) were obtained by temporal interpolation; as a result, the relative center locations are not necessarily accurate. The 1-km RMW in (c) and the 5-km RMWs in (b), (c), and (d) were also obtained by temporal interpolation. Note that the rainfall distribution, in particular that on the north side of Noul, has been artificially affected by radar attenuation.

plot period B (Fig. 11b), a concave portion, along the inner edge of the eyewall, which was ~20 km northeast of the storm center during period A, was northwest of the center and inside an active convective asymmetry with reflectivity greater than 40 dBZ that extended from southwest to northeast. In the concave portion, SR wind speed was weak, below 10 m s^{-1}, and a potential cyclonic circulation was forming at around 10 km northwest of the storm center. From period A to period B, SR wind speed increased on the left side of the track, except in the concave portion. During period C, a small-scale cyclonic circulation was found southwest of the storm center. Hereafter, we refer to this local circulation as a mesovortex. During period D, the mesovortex moved counterclockwise along the inner edge of the eyewall (Fig. 11d).

The mesovortex was characterized by a SLP minimum and a high-θ_e peak, as seen in the surface observation

time series obtained at Nakasuji station on Tarama Island (Fig. 12). These time series show the inner-core structure of Noul at the surface from downshear to upshear, because during period II Noul was moving northeastward with a speed greater than 18 m s^{-1} and it passed very near Tarama Island. From 1527 to 1531 UTC, when the mesovortex made its nearest approach to Tarama Island (Fig. 10c), the sign of the SR tangential winds v_{SR} changed (Fig. 12a); in addition, θ_e reached ~368 K, and SLP fell to ~981 hPa (Fig. 12c). The locations of the SLP minimum and the high-θ_e peak were displaced from the storm center by 15–20 km toward the active convective asymmetry (Fig. 12b). The radial profiles of θ_e and SLP within 35 km from the storm center were distorted from symmetry, suggesting that the scale of the mesovortex was ~15 km, much smaller than the RMW (~27 km) and the radius of maximum
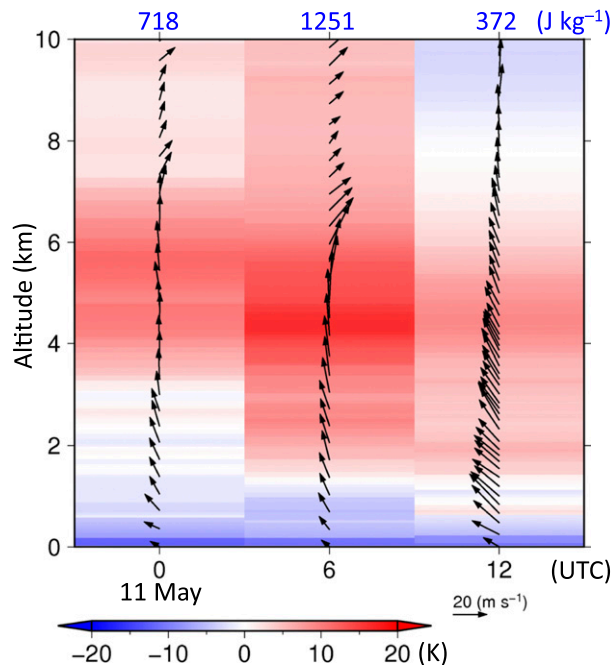
FIG. 10. Vertical profiles of the difference between the equivalent potential temperature θ_e averaged over the lowest 500 m and the saturated equivalent potential temperature θ_{es} at each altitude from sonde observations at Ishigaki Island (see Fig. 2a). The warm colors denote vertical levels where the parcel's θ_e below 500 m exceeds the surrounding environment's θ_{es}. Convective available potential energy (CAPE), which is calculated by lifting a parcel averaged over the lowest 500 m, is shown on the top of the panel.

rainfall (~40 km). From 1533 to 1541 UTC, just prior to the passage of the active convective asymmetry over Nakasuji (Fig. 12b), a steep horizontal gradient of θ_e was observed, reaching 15 K $(10 \, \text{km})^{-1}$, in the area of outflow (Fig. 12a), indicative of positive θ_e advection from the eye into the convection.

At 1621 UTC, the PPI pattern at an elevation angle of 0.2° showed that the $0 \, \text{m s}^{-1}$ isopleth of V_D was nearly perpendicular to the radar range direction in the vicinity of the convective asymmetry on the west side of Noul (Fig. 3b, dashed oval).[3] This orientation implies the existence of horizontal convergence along the convective area. The V_D height in the convergence area in Fig. 3b is 1–2 km. This configuration, that is, positive θ_e advection inside the eyewall and convergence along the convective area, was favorable for the maintenance of the convection upshear. Because SR outflow was observed radially outside the convection upshear (Fig. 11), we speculate that the maintenance of the convection on the upshear

side could not have been realized without the advection of high-θ_e air from the eye region by the mesovortex.

Guimond et al. (2016) reported, on the basis of aircraft observations of Hurricane Karl (2010), a similar configuration of a mesovortex in the eye and convective bursts in the eyewall. They showed that convective bursts occurred in an area of low-level convergence of outflow with warm buoyant air associated with mesovortices in the eye and vortex-scale flow. Eastin et al. (2005) reported, on the basis of aircraft observations, the origin of buoyant updrafts in the eyewall appeared to be high-θ_e air advected outward by mesovortices from the eye, where θ_e was much (~10 K) greater than that in the eyewall. Reasor et al. (2009) speculated that the mixing of warm, moist air from the eye offset the negative influence of relatively strong shear and led to the rapid intensification (RI) of Hurricane Guillermo (1997).

In Noul, relatively strong SR tangential winds of greater than $30 \, \text{m s}^{-1}$ were present at the inner edge of the convection (Figs. 12a,b). Using the SR tangential winds observed at Tarama Island and the following formula for relative vorticity:

$$\zeta = \frac{\partial v_{\text{SR}}}{\partial r} + \frac{v_{\text{SR}}}{r},$$

we calculated that relative vorticity at the inner edge of the convection reached $0.8 \times 10^{-2} \, \text{s}^{-1}$.[4] Near the mesovortex, a maximum gust wind speed of $58.6 \, \text{m s}^{-1}$ (earth-relative wind) was observed at Shimoji (Figs. 2a and 11d). This very strong wind was also confirmed by the V_D of greater than $60 \, \text{m s}^{-1}$ at 1–2-km altitude (Fig. 3b). A similar very strong wind along the inside edge of the eyewall was also observed in Hurricane Hugo (1989) (Marks et al. 2008).

6. Vortex tilt

a. Wavenumber-1 reflectivity asymmetry

Wavenumber-0–7[5] reflectivities averaged over radii of 25–50 km (around the contracting RMW and outside the RMW) showed that a wavenumber-1 reflectivity asymmetry with amplitude greater than 10 dBZ was present until 1625 UTC (Fig. 13). The radial range in Fig. 13 was determined from the dominant region of wavenumber-1 asymmetry from 1330 to 1600 UTC (Figs. 14a–d); during this period, a positive wavenumber-1 anomaly propagated

---

[3] Note that V_D is the Earth-relative wind velocity, not the SR wind velocity.

[4] Note that the calculated vorticity results from the superposition of Noul primary vortex and the mesovortex.

[5] Note that since the storm center was defined as the center at 1-km altitude, the reflectivity asymmetry is shown with respect to the vortex at 1-km altitude.
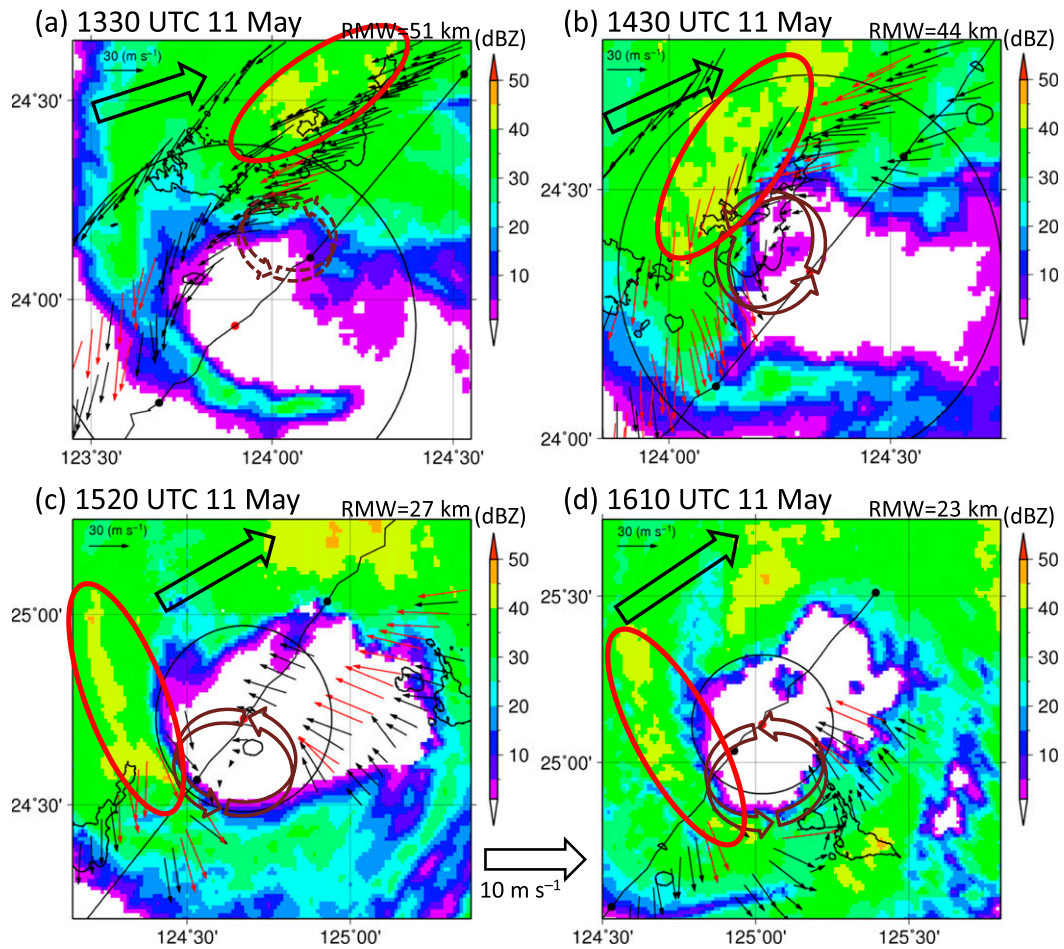
FIG. 11. Distribution of storm-relative (SR) surface winds (small arrows: red $\geq 36\,\mathrm{m\,s^{-1}}$ and black $< 36\,\mathrm{m\,s^{-1}}$) and composite radar reflectivity (color scale) at (a) 1330, (b) 1430, (c) 1520, and (d) 1610 UTC 11 May. SR winds observed at each weather station during each period shown in Table 1 are plotted at their location relative to the TC center position at each specific time. The black line is the track determined by the GBVTD-simplex method until 1700 UTC 11 May. The red ellipse indicates the area of active asymmetric convection on which this study focused. The bold black arrow shows the 850–200-hPa shear vector. The black circle denotes the 1-km RMW. The dashed arrow circle indicates the concave portion of the inner edge of the eyewall. The brown arrow circle indicates the location of a possible mesovortex. The 1-km RMW indicated in (b) was obtained by a temporal interpolation.

cyclonically from the downshear-left side to the up-shear side at an almost single phase speed between radii of 25 and 50 km. The propagation speed is discussed further in section 6c. After 1600 UTC, the wavenumber-1 asymmetry between the radii of 25 and 50 km rapidly decreased (Fig. 13), and there was no significant wavenumber-1 asymmetry within a 70-km radius, except around the 20-km radius, where the deviation from a closed eyewall caused an asymmetry (Fig. 14e). Instead, wavenumber-0 reflectivity rapidly

TABLE 1. Plot periods for the analysis of storm-relative (SR) surface winds at four specific times (Fig. 11). Note that not all SR winds observed at each weather station are plotted during the plot periods. If a weather station was located in the eye during any two plot periods, then SR winds in the eye were plotted during the period closer to the observed time.

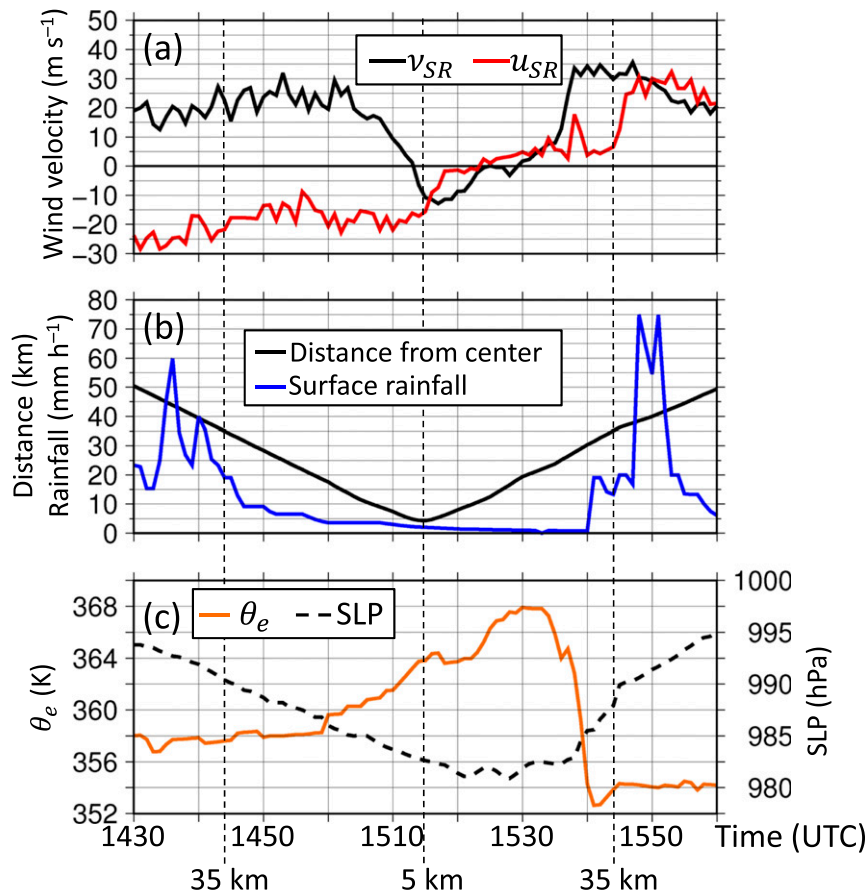|	Specific times	Plot periods	Location of the convective asymmetry
A	1330 UTC 11 May	1230–1430 UTC	North-northeast of Noul
B	1430 UTC 11 May	1330–1530 UTC	Northwestern side of Noul
C	1520 UTC 11 May	1450–1600 UTC	Western side of Noul
D	1610 UTC 11 May	1530–1640 UTC	Southwestern side of Noul

FIG. 12. Time evolutions of surface observations at Nakasuji (location shown in Fig. 2a). (a) Storm-relative surface tangential wind velocity v_{SR} (m s^{-1}, black line) and radial wind velocity u_{SR} (m s^{-1}, red line). (b) Distance between the storm-scale center and the weather station (km, black line) and surface rainfall (mm h^{-1}, blue line). (c) Equivalent potential temperature θ_e (K, orange line) and sea level pressure (SLP) (hPa, black dashed line). The dashed vertical lines refer to the distance from the storm center shown in (b).

increased with time, becoming dominant by 1700 UTC (Fig. 13).

b. Tilt evolution

We examined the evolution of vortex tilt in relation to the wavenumber-1 reflectivity asymmetry. The tilt direction of the inner-core vortex (on the scale of the RMW) between the center at 1-km altitude and that at 5-km altitude was almost the same as that of the positive wavenumber-1 reflectivity from 1230 to 1330 UTC (Fig. 15). Note that before 1330 UTC the positive wavenumber-1 asymmetry was mainly found in the downshear-left quadrant outside the 50-km radius (Fig. 14a). After 1330 UTC the tilt was 45°–90° downstream of the wavenumber-1 reflectivity, reaching the upshear-right quadrant, though with erratic fluctuations (Fig. 15). Note, however, that there exists uncertainty in the analysis of the vortex tilt because the quality of the

GBVTD analysis was poor, particularly during period II. According to Rogers et al. (2003) and Reasor et al. (2013), both the upward motion maximum and the tilt direction tend to be found upstream of the rainfall maximum. In Noul, the azimuthal location of the vortex tilt coincided with that of the mesovortex during period II (Fig. 15). The center locations at 5-km altitude detected by the center-finding algorithm were systematically displaced toward the location of the mesovortex. The tilt precession might have been partly due to the cyclonic propagation of the mesovortex because the very strong wind speeds greater than 50 m s^{-1}, which are suggestive of the mesovortex, were observed even at 5-km altitude (not shown).

The tilt magnitude was relatively large ($\sim$5–15 km) when the wavenumber-1 reflectivity was strong (1200–1600 UTC) (Figs. 16a,b). After 1600 UTC, however, when the vortex tilted upshear, the tilt magnitude rapidly
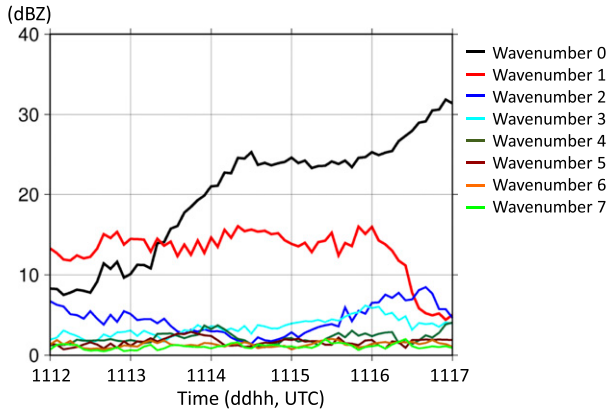
FIG. 13. Time evolution of wavenumber-0–7 radar reflectivity averaged over radii of 25–50 km (simple averages were computed without considering the areal mean). The reflectivity is averaged between 1- and 2-km altitudes.

decreased to below 4 km; this reduction in the magnitude indicates that the vortex was nearly aligned after its upshear precession from the downshear-left quadrant in strong shear (Fig. 16a). This alignment occurred at the same time as the drop in the amplitude of the wavenumber-1 reflectivity asymmetry (Fig. 16b).

Previous studies have shown that maximum upward motion occurs downtilt (e.g., Braun et al. 2006; Ueno 2008) and that the amplitude of the wavenumber-1 upward motion asymmetry in the eyewall is strongly correlated with the amplitude of the wavenumber-1 rainfall asymmetry (Ueno 2007). Therefore, it is plausible that the formation of the closed eyewall of Noul was associated with the alignment of the vortex after 1600 UTC.

c. Comparison with theory

We further examined the vortex tilt in the context of a tilt mode of VRWs in shear (Reasor et al. 2004; Reasor and Montgomery 2015). The wavenumber-1 asymmetry was primarily observed between radii of 25 and 50 km (Fig. 13), where the radial gradient of relative vorticity at 1-km altitude was negative (Fig. 17). This negative radial gradient would allow VRWs to propagate upwind relative to the tangential wind, under the assumption that the radial gradient of vorticity has the same sign as the radial gradient of PV. In fact, the wavenumber-1 convective asymmetry at a radius of 37.5 km propagated cyclonically at an earth-relative speed of $8.9\,\mathrm{m\,s^{-1}}$, which was ~24% of the corresponding $\bar{v}$ at 1-km altitude ($37.2\,\mathrm{m\,s^{-1}}$, averaged over 25–50-km radius) during the
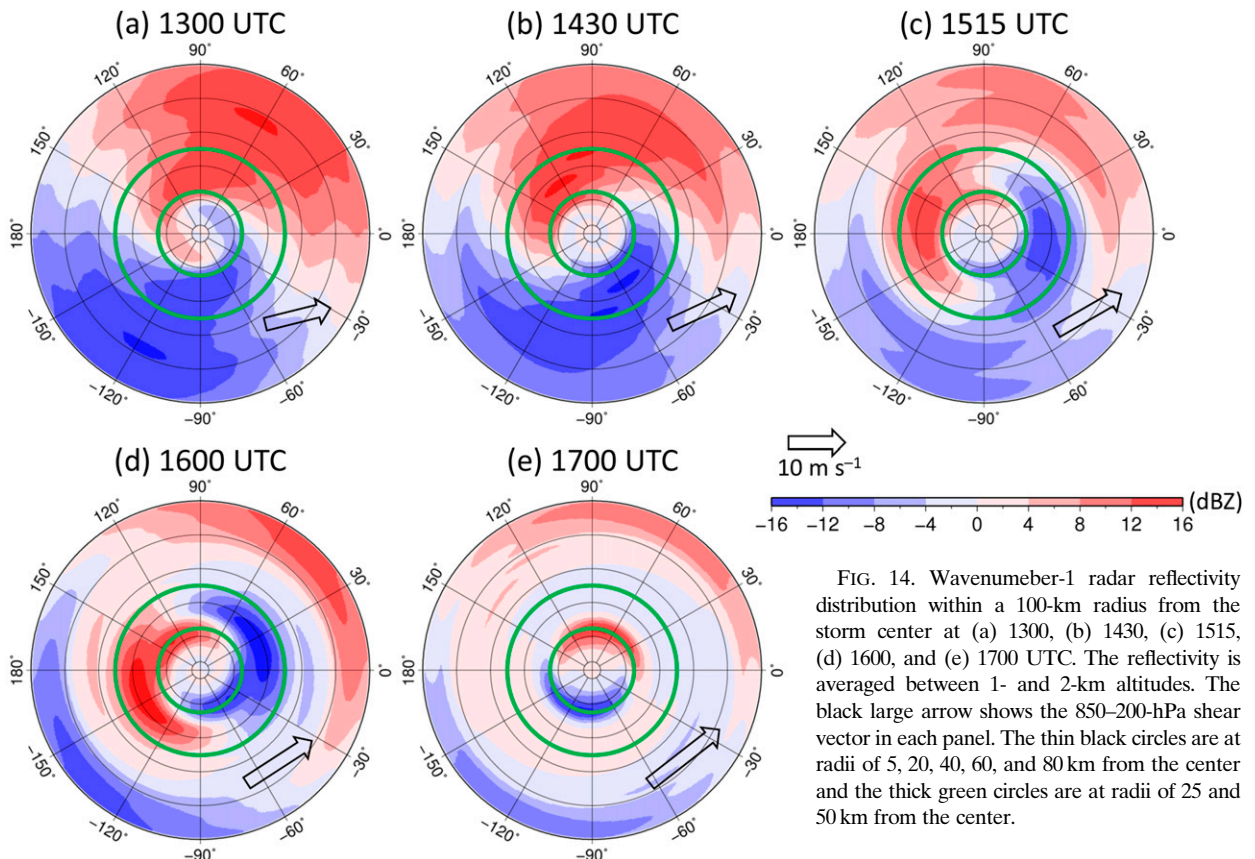

FIG. 14. Wavenumeber-1 radar reflectivity distribution within a 100-km radius from the storm center at (a) 1300, (b) 1430, (c) 1515, (d) 1600, and (e) 1700 UTC. The reflectivity is averaged between 1- and 2-km altitudes. The black large arrow shows the 850–200-hPa shear vector in each panel. The thin black circles are at radii of 5, 20, 40, 60, and 80 km from the center and the thick green circles are at radii of 25 and 50 km from the center.
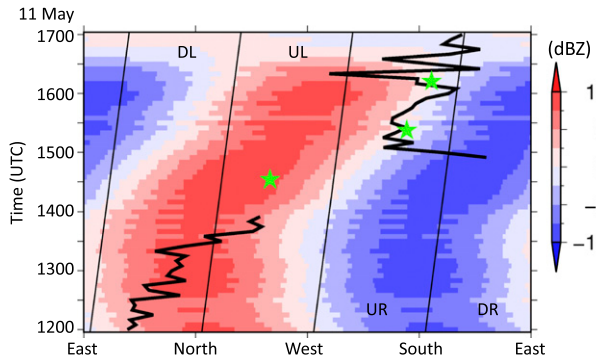
FIG. 15. Time–azimuthal distribution of wavenumber-1 reflectivity averaged between radii of 25 and 50 km, and between 1- and 2-km altitudes. The thick black line indicates the direction of the vortex tilt determined from the difference in the center location between 1- and 5-km altitudes. The slanting lines divide the shear quadrants. "DL," "UL," "UR," and "DR" denote downshear-left, upshear-left, upshear-right, and downshear-right quadrants, respectively. The green stars indicate the direction of the mesovortex from the storm center.

period from 1330 to 1630 UTC. This fact may allow the observed wavenumber-1 asymmetry to be interpreted as a tilt mode of VRWs.

To what degree is the observed, possible tilt mode consistent with theory? The behavior of the tilt mode depends on the radial gradient of PV at the critical radius, as described in the introduction. Unfortunately, we could not confirm the sign of the gradient at the critical

radius, which was located outside the analysis domain (Fig. 17). If damping of the tilt mode is absent, the vortex can be aligned through its precession upshear; this process matches Noul's actual behavior. Reasor and Montgomery (2015) derived a heuristic model of a tilt mode without damping in cylindrical coordinates (r, φ, z, t), where φ is the azimuthal angle (counterclockwise), z is the pseudoheight vertical coordinate (Hoskins and Bretherton 1972), and t is time, as follows:

$$q'(r, \varphi, z, t) \approx -\frac{2U}{\omega_p} \frac{d\overline{q}}{dr} \sin\left(\frac{\omega_p t}{2}\right) \cos\left(\varphi - \frac{\omega_p t}{2}\right) \cos\left(\frac{\pi z}{H}\right),$$

$$(1)$$

where $\overline{q}$ and q' are the axisymmetric and asymmetric components of PV, respectively; U is half the magnitude of the vertical shear; ω_p is the vortex precession frequency; and H is the depth of the vortex. The tilt is maximized at $\varphi = \pi/2$ (90° to the left of shear), and the tilt magnitude between the surface and half of H can be estimated as $|r'| \equiv |q'/(d\overline{q}/dr)| = |2U/\omega_p|$. The vortex precession frequency ω_p is expressed as double the frequency of the observed wavenumber-1 VRW, $2 \times (V/R)$, where V is the observed wavenumber-1 VRW propagation speed ($\sim 9\,\mathrm{m\,s^{-1}}$) and R is the mean radius of the wave ($\sim 37.5\,\mathrm{km}$). Since vertical shear was $\sim 13\,\mathrm{m\,s^{-1}}$ at 1500 UTC, U is $6.5\,\mathrm{m\,s^{-1}}$. Substituting these values into $|2U/\omega_p|$ yields $|r'| = \sim 27\,\mathrm{km}$. If it is assumed that H is $\sim 12\,\mathrm{km}$, which is equivalent to the height of ~ 200-hPa
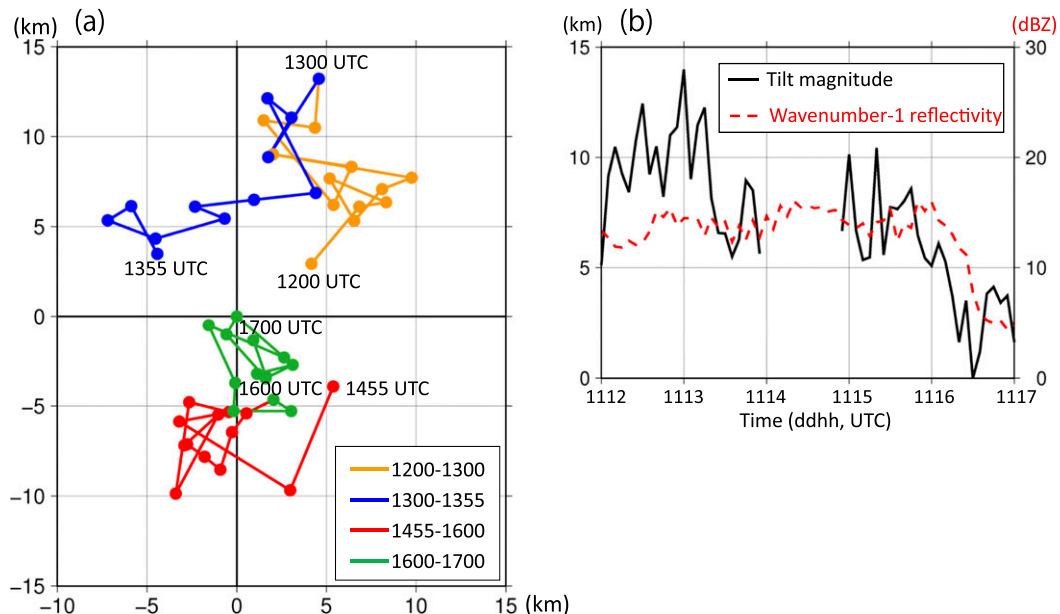

FIG. 16. Time evolution of (a) tilt direction and (b) magnitude determined from differences in the center location between 1- and 5-km altitudes. In (a), the origin of the plot is the storm center at 1-km altitude and the displacement of the 5-km center relative to the 1-km center is drawn.
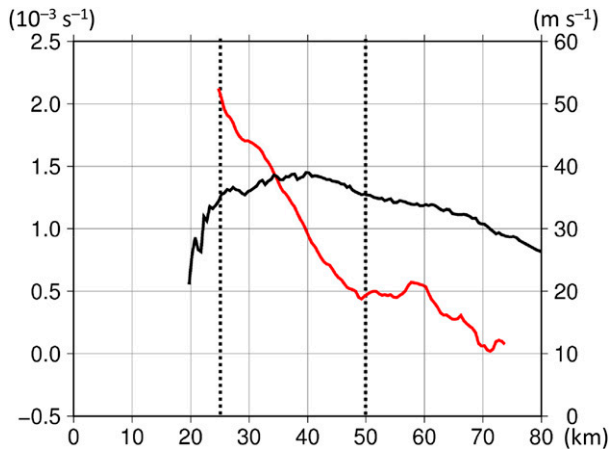
FIG. 17. Radial profiles of time-averaged (from 1330 to 1630 UTC) azimuthal-mean relative vorticity (red line, left axis) and $\bar{v}$ at 1-km altitude (black line, right axis). After the time averaging, the relative vorticity values were radially filtered using a 5-km running mean. The vertical dotted lines indicate the radial range from 25 to 50 km.

level (according to sonde observations at Ishigaki Island), and that the tilt magnitude increases linearly with height, then the tilt magnitude between 1- and 5-km altitudes ($\Delta z = 4$ km) is estimated to be $(2|r'|\Delta z)/H = \sim 18$ km.

This estimate is much larger than the actual tilt magnitude (~ 7.5 km) at around 1500 UTC (Fig. 16b). A possible explanation for this difference is that the local shear in the inner core of the vortex was much less than the estimated value of U. In addition, processes such as axisymmetrization (e.g., Enagonio and Montgomery 2001), diabatic PV production (DeMaria 1996; Davis et al. 2008), and stretching, and upward advection, of vorticity (Nguyen and Molinari 2015; Miyamoto and Nolan 2018), may have decreased the tilt magnitude.

After 1700 UTC, the eyewall structure remained nearly symmetric for a few hours (Fig. 9f). This fact suggests that damping of the tilt mode occurred. If so, the magnitude of the downshear-left equilibrium tilt can be estimated as $|r'| \equiv |q'/(d\bar{q}/dr)| = |U/\omega_p|$ [Eq. (14) of Reasor and Montgomery (2015)]. By 1700 UTC, vertical shear was ~ 15 m s^{-1}. For ω_p, $\bar{v}$ is assumed to have increased by ~ 5 m s^{-1} (Fig. 5), and this increase leads to an increase in V (14 m s^{-1}). Here R is assumed to have contracted to ~ 30 km as the RMW contracted. Thus, the tilt magnitude between 1- and 5-km altitudes is estimated to be ~ 5 km. This large decrease in the theoretical tilt magnitude is consistent with the decrease in the observed tilt magnitude.

7. Discussion

Noul's reintensification was characterized by convective bursts, vertical alignment of the vortex following its precession upshear, and the formation of a closed eyewall in an environment of increasing shear caused by an approaching upper-level trough. Here, these features are compared with features of other intensifying TCs in strong shear.

a. Intensification in strong shear

Some previous studies have suggested that strong shear can favorably contribute to TC intensification through processes such as downshear reformation or asymmetric intensification. Nguyen and Molinari (2015) showed through a numerical simulation of Tropical Storm Gabrielle (2001) that during RI, an upright, intense mesovortex formed downshear by vorticity stretching in a sufficiently moist environment, and that the mesovortex evolved into the TC vortex as its flow axisymmetrized the original vortex. Meanwhile, Musgrave et al. (2008) performed numerical experiments of Gabrielle and showed that when vertical shear was reduced, the simulated intensity was weaker than the actual intensity. None of these cases of asymmetric intensification, however, was accompanied by a closed eyewall.

In Noul, similar to other intensifying TCs, the timing of the increase in $\bar{v}$ was consistent with the timing of the increase in azimuthal-mean reflectivity inside the RMW (Fig. 7c). This result suggests that the increase in the axisymmetric component of diabatic heating through asymmetric convection was important for Noul's reintensification, as described by Molinari and Vollaro (2010) and Nguyen and Molinari (2012). The convective bursts initially occurred in a favorable thermodynamic environment in the downshear-left quadrant (sections 5a). The tilt direction of the inner-core vortex was also in the downshear-left quadrant at that time (section 6b). If adiabatic upward motion was forced on the downtilt side in response to increasing shear (Jones 1995; Ueno 2007), it is plausible that the increase in shear around the onset of reintensification caused Noul to tilt, and triggered the convective bursts. When the convection propagated upshear, the advection of high-θ_e air from the eye by the mesovortex likely contributed to the maintenance of the convection (section 5b).

With regard to the vertical alignment during intensification, it might be useful to consider Hurricane Earl (2010) because, similar to Noul, Earl became vertically aligned after being significantly tilted to 90° left of shear (Stevenson et al. 2014; Rogers et al. 2015; Susca-Lopata et al. 2015). Earl was characterized by a displacement of ~ 50 km between circulation centers at 2- and 8-km altitudes prior to RI in moderate shear. Over the next 12 h, RI and the vertical alignment of the vortex occurred in conjunction with convective bursts inside the RMW. Chen and Gopalakrishnan (2015) showed

through numerical simulation that Earl was aligned after the onset of RI, a result that is consistent with the alignment of Noul during its reintensification. An important difference, however, is that Earl continued to rapidly intensify into a major hurricane, whereas Noul began to weaken again shortly afterward because of low ocean temperatures (Fig. 1a) and strong shear more than $16 \, \mathrm{m \, s^{-1}}$ (Fig. 6).

b. Effect of an upper-level trough

It has been shown that TCs can intensify through interaction with an upper-level trough and associated jet (Molinari and Vollaro 1990; DeMaria et al. 1993; Hanley et al. 2001), though a more recent study by Peirano et al. (2016) cast doubt on the positive influence of troughs on TCs. An upper-level jet preferably transfers negative angular momentum outward to spin up the outflow layer of the TC. The eddy momentum flux convergence (EFC) is defined as follows:

$$\mathrm{EFC} \equiv -\frac{1}{r^2} \frac{\partial}{\partial r} r^2 \overline{u'_{\mathrm{SR}} v'_{\mathrm{SR}}}, \qquad (2)$$

where u_{SR} is the storm-relative radial wind, the overbar indicates the azimuthal mean, and the primes indicate the deviation from the azimuthal mean. To indicate a trough interaction objectively, Hanley et al. (2001) used as an indicator an EFC averaged over a 300–600-km radial range at the 200-hPa level that exceeds $10 \, \mathrm{m \, s^{-1} \, day^{-1}}$ continuously for more than 12 h.

An upper-level jet axis associated with a deep trough was located ~1500 km north of Noul when the convective bursts started at around 1000 UTC 11 May (not shown). We calculated EFC at each radius by using JRA-55 reanalysis data and found that the radius where it exceeded $10 \, \mathrm{m \, s^{-1} \, day^{-1}}$ was ~850 km from Noul's center as of 1200 UTC (not shown); thus, the trough was too far away to spin up Noul. Therefore, from the perspective of EFC, we could not conclude that Noul reintensified through interaction with the upper-level trough.

8. Conclusions

Typhoon Noul (2015) underwent reintensification and developed a closed eyewall during its passage near Ishigaki Island from 1000 to 1800 UTC 11 May 2015. During this period, westerly to southwesterly vertical wind shear increased from 11 to $16 \, \mathrm{m \, s^{-1}}$ and the speed of Noul's northeastward movement increased from 10 to $20 \, \mathrm{m \, s^{-1}}$. The evolution of Noul during this period was atypical, because strong vertical shear is generally unfavorable for intensification and tends to induce an asymmetric eyewall structure. Surface observations around

Ishigaki Island and operational Doppler radar data provided an opportunity to document Noul's reintensification. We therefore examined why Noul reintensified and why it had a closed eyewall in strong shear.

The evolution of the azimuthal-mean structure showed that, in association with the occurrence of convective bursts, inflow penetrated into a radius of ~40 km, well inside the RMW, at least below 4-km altitude, and azimuthal-mean reflectivity inside the RMW increased. Further, the maximum $\bar{v}$ at 2-km altitude rapidly increased from 30 to $45 \, \mathrm{m \, s^{-1}}$ during only 5 h and the 1-km RMW contracted from ~65 to ~40 km. These features are consistent with those of intensifying TCs reported by previous studies.

The convective bursts were dominated by a positive wavenumber-1 asymmetry in the downshear-left quadrant. The asymmetry between the radii of 25 and 50 km was organized into the eyewall and rotated cyclonically to the upshear side. In conjunction with the convective asymmetry, the direction of the vortex tilt between 1- and 5-km altitudes rotated cyclonically from the downshear-left to the upshear-right quadrant while the tilt magnitude decreased to less than 4 km. The amplitude of the wavenumber-1 convective asymmetry also decreased and a closed eyewall formed. These features indicate that after the vortex precessed cyclonically into the upshear-right quadrant in strong shear, the vortex was vertically aligned. This behavior is qualitatively consistent with the theory that TC vortices can resist tilting by vertical shear.

Surface observations showed that a mesovortex occurred inside the convective asymmetry on the upshear side. The mesovortex was characterized by warm moist air and a pressure minimum, and the horizontal gradient of θ_e between the mesovortex and the convective asymmetry reached $15 \, \mathrm{K} \, (10 \, \mathrm{km})^{-1}$. The configuration of the mesovortex was thus favorable for the advection of high-θ_e air from the eye to the active convective region on the upshear side of the storm.

The results of our analysis suggest that the vortex tilt, convective bursts, and subsequent intensification were triggered by the increase in vertical shear in a convectively favorable environment. To our knowledge, this study is the first one based on high-temporal-resolution observations of a TC that was vertically aligned as it precessed upshear during intensification. Although many observational studies have examined the relationships among shear, an asymmetric structure, and intensity change, few studies have examined the dramatic changes of a TC vortex occurring on a short time scale, ~6 h, in response to an increase in shear. Future studies should examine further the effects of shear on TCs on the basis of high-temporal-resolution observations and simulations.

REFERENCES

Bell, M. M., and W. Lee, 2012: Objective tropical cyclone center tracking using single-Doppler radar. *J. Appl. Meteor. Climatol.*, **51**, 878–896, https://doi.org/10.1175/JAMC-D-11-0167.1.

Bender, M. A., 1997: The effect of relative flow on the asymmetric structure in the interior of hurricanes. *J. Atmos. Sci.*, **54**, 703–724, https://doi.org/10.1175/1520-0469(1997)054<0703:TEORFO>2.0.CO;2.

Black, M. L., J. F. Gamache, F. D. Marks, C. E. Samsury, and H. E. Willoughby, 2002: Eastern Pacific Hurricanes Jimena of 1991 and Olivia of 1994: The effect of vertical shear on structure and intensity. *Mon. Wea. Rev.*, **130**, 2291–2312, https://doi.org/10.1175/1520-0493(2002)130<2291:EPHJOA>2.0.CO;2.

Bolton, D., 1980: The computation of equivalent potential temperature. *Mon. Wea. Rev.*, **108**, 1046–1053, https://doi.org/10.1175/1520-0493(1980)108<1046:TCOEPT>2.0.CO;2.

Braun, S. A., and L. Wu, 2007: A numerical study of Hurricane Erin (2001). Part II: Shear and the organization of eyewall vertical motion. *Mon. Wea. Rev.*, **135**, 1179–1194, https://doi.org/10.1175/MWR3336.1.

——, M. T. Montgomery, and Z. Pu, 2006: High-resolution simulation of Hurricane Bonnie (1998). Part I: The organization of eyewall vertical motion. *J. Atmos. Sci.*, **63**, 19–42, https://doi.org/10.1175/JAS3598.1.

Chen, H., and S. G. Gopalakrishnan, 2015: A study on the asymmetric rapid intensification of Hurricane Earl (2010) using the HWRF system. *J. Atmos. Sci.*, **72**, 531–550, https://doi.org/10.1175/JAS-D-14-0097.1.

Chen, S., J. A. Knaff, and F. D. Marks Jr., 2006: Effects of vertical wind shear and storm motion on tropical cyclone rainfall asymmetries deduced from TRMM. *Mon. Wea. Rev.*, **134**, 3190–3208, https://doi.org/10.1175/MWR3245.1.

Corbosiero, K. L., and J. Molinari, 2002: The effects of vertical wind shear on the distribution of convection in tropical cyclones. *Mon. Wea. Rev.*, **130**, 2110–2123, https://doi.org/10.1175/1520-0493(2002)130<2110:TEOVWS>2.0.CO;2.

——, and ——, 2003: The relationship between storm motion, vertical wind shear, and convective asymmetries in tropical cyclones. *J. Atmos. Sci.*, **60**, 366–376, https://doi.org/10.1175/1520-0469(2003)060<0366:TRBSMV>2.0.CO;2.

——, ——, A. R. Aiyyer, and M. L. Black, 2006: The structure and evolution of Hurricane Elena (1985). Part II: Convective asymmetries and evidence for vortex Rossby waves. *Mon. Wea. Rev.*, **134**, 3073–3091, https://doi.org/10.1175/MWR3250.1.

Davis, C. A., S. C. Jones, and M. Riemer, 2008: Hurricane vortex dynamics during Atlantic extratropical transition. *J. Atmos. Sci.*, **65**, 714–736, https://doi.org/10.1175/2007JAS2488.1.

DeHart, J. C., R. A. Houze, and R. F. Rogers, 2014: Quadrant distribution of tropical cyclone inner-core kinematics in relation to environmental shear. *J. Atmos. Sci.*, **71**, 2713–2732, https://doi.org/10.1175/JAS-D-13-0298.1.

DeMaria, M., 1996: The effect of vertical shear on tropical cyclone intensity change. *J. Atmos. Sci.*, **53**, 2076–2088, https://doi.org/10.1175/1520-0469(1996)053<2076:TEOVSO>2.0.CO;2.

——, 2009: A simplified dynamical system for tropical cyclone intensity prediction. *Mon. Wea. Rev.*, **137**, 68–82, https://doi.org/10.1175/2008MWR2513.1.

——, and J. Kaplan, 1994: A Statistical Hurricane Intensity Prediction Scheme (SHIPS) for the Atlantic basin. *Wea. Forecasting*, **9**, 209–220, https://doi.org/10.1175/1520-0434(1994)009<0209:ASHIPS>2.0.CO;2.

——, and ——, 1999: An updated Statistical Hurricane Intensity Prediction Scheme (SHIPS) for the Atlantic and eastern North Pacific basins. *Wea. Forecasting*, **14**, 326–337, https://doi.org/10.1175/1520-0434(1999)014<0326:AUSHIP>2.0.CO;2.

——, J.-J. Baik, and J. Kaplan, 1993: Upper-level eddy angular momentum flux and tropical cyclone intensity change. *J. Atmos. Sci.*, **50**, 1133–1147, https://doi.org/10.1175/1520-0469(1993)050<1133:ULEAMF>2.0.CO;2.

Eastin, M. D., W. M. Gray, and P. G. Black, 2005: Buoyancy of convective vertical motions in the inner core of intense hurricanes. Part II: Case studies. *Mon. Wea. Rev.*, **133**, 209–227, https://doi.org/10.1175/MWR-2849.1.

Enagonio, J., and M. T. Montgomery, 2001: Tropical cyclogenesis via convectively forced vortex Rossby waves in a shallow water primitive equation model. *J. Atmos. Sci.*, **58**, 685–706, https://doi.org/10.1175/1520-0469(2001)058<0685:TCVCFV>2.0.CO;2.

Frank, W. M., and E. A. Ritchie, 1999: Effects of environmental flow upon tropical cyclone structure. *Mon. Wea. Rev.*, **127**, 2044–2061, https://doi.org/10.1175/1520-0493(1999)127<2044:EOEFUT>2.0.CO;2.

——, and ——, 2001: Effects of vertical wind shear on the intensity and structure of numerically simulated hurricanes. *Mon. Wea. Rev.*, **129**, 2249–2269, https://doi.org/10.1175/1520-0493(2001)129<2249:EOVWSO>2.0.CO;2.

Guimond, S. R., G. M. Heymsfield, P. D. Reasor, and A. C. Didlake, 2016: The rapid intensification of Hurricane Karl (2010): New remote sensing observations of convective bursts from the Global Hawk platform. *J. Atmos. Sci.*, **73**, 3617–3639, https://doi.org/10.1175/JAS-D-16-0026.1.

Hanley, D., J. Molinari, and D. Keyser, 2001: A composite of the interactions between tropical cyclones and upper-tropospheric troughs. *Mon. Wea. Rev.*, **129**, 2570–2584, https://doi.org/10.1175/1520-0493(2001)129<2570:ACSOTI>2.0.CO;2.

Harasti, P. R., C. J. McAdie, P. P. Dodge, W.-C. Lee, J. Tuttle, S. T. Murillo, and F. D. Marks, 2004: Real-time implementation of single-Doppler radar analysis methods for tropical cyclones: Algorithm improvements and use with WSR-88D display data. *Wea. Forecasting*, **19**, 219–239, https://doi.org/10.1175/1520-0434(2004)019<0219:RIOSRA>2.0.CO;2.

Hoskins, B. J., and F. P. Bretherton, 1972: Atmospheric frontogenesis models: Mathematical formulation and solution. *J. Atmos. Sci.*, **29**, 11–37, https://doi.org/10.1175/1520-0469(1972)029<0011:AFMMFA>2.0.CO;2.

JMA, 2016: Annual report on the activities of the RSMC Tokyo-Typhoon Center. Japan Meteorological Agency, 103 pp., http://www.jma.go.jp/jma/jma-eng/jma-center/rsmc-hp-pub-eg/AnnualReport/2015/Text/Text2015.pdf.

Jones, S. C., 1995: The evolution of vortices in vertical shear. I: Initially barotropic vortices. *Quart. J. Roy. Meteor. Soc.*, **121**, 821–851, https://doi.org/10.1002/qj.49712152406.

Kaplan, J., and M. DeMaria, 2003: Large-scale characteristics of rapidly intensifying tropical cyclones in the North Atlantic

basin. *Wea. Forecasting*, **18**, 1093–1108, https://doi.org/10.1175/1520-0434(2003)018<1093:LCORIT>2.0.CO;2.

——, ——, and J. A. Knaff, 2010: A revised tropical cyclone rapid intensification index for the Atlantic and eastern North Pacific basins. *Wea. Forecasting*, **25**, 220–241, https://doi.org/10.1175/2009WAF2222280.1.

Knaff, J. A., C. R. Sampson, and M. DeMaria, 2005: An operational statistical typhoon intensity prediction scheme for the western North Pacific. *Wea. Forecasting*, **20**, 688–699, https://doi.org/10.1175/WAF863.1.

Kobayashi, S., and Coauthors, 2015: The JRA-55 Reanalysis: General specifications and basic characteristics. *J. Meteor. Soc. Japan*, **93**, 5–48, https://doi.org/10.2151/jmsj.2015-001.

Lamb, H., 1932: *Hydrodynamics*. 6th ed. Dover, 732 pp.

Lee, W.-C., and F. D. Marks Jr., 2000: Tropical cyclone kinematic structure retrieved from single-Doppler radar observations. Part II: The GBVTD-simplex center finding algorithm. *Mon. Wea. Rev.*, **128**, 1925–1936, https://doi.org/10.1175/1520-0493(2000)128<1925:TCKSRF>2.0.CO;2.

——, B. J.-D. Jou, P.-L. Chang, and S.-M. Deng, 1999: Tropical cyclone kinematic structure retrieved from single-Doppler radar observations. Part I: Interpretation of Doppler velocity patterns and the GBVTD technique. *Mon. Wea. Rev.*, **127**, 2419–2439, https://doi.org/10.1175/1520-0493(1999)127<2419:TCKSRF>2.0.CO;2.

Marks, F. D., P. G. Black, M. T. Montgomery, and R. W. Burpee, 2008: Structure of the eye and eyewall of Hurricane Hugo (1989). *Mon. Wea. Rev.*, **136**, 1237–1259, https://doi.org/10.1175/2007MWR2073.1.

Miyamoto, Y., and D. Nolan, 2018: Structural changes preceding rapid intensification in tropical cyclones as shown in a large ensemble of idealized simulations. *J. Atmos. Sci.*, **75**, 555–569, https://doi.org/10.1175/JAS-D-17-0177.1.

Molinari, J., and D. Vollaro, 1990: External influences on hurricane intensity. Part II: Vertical structure and response of the hurricane vortex. *J. Atmos. Sci.*, **47**, 1902–1918, https://doi.org/10.1175/1520-0469(1990)047<1902:EIOHIP>2.0.CO;2.

——, and ——, 2010: Rapid intensification of a sheared tropical storm. *Mon. Wea. Rev.*, **138**, 3869–3885, https://doi.org/10.1175/2010MWR3378.1.

——, P. Dodge, D. Vollaro, K. L. Corbosiero, and F. Marks, 2006: Mesoscale aspects of the downshear reformation of a tropical cyclone. *J. Atmos. Sci.*, **63**, 341–354, https://doi.org/10.1175/JAS3591.1.

Murillo, S. T., W.-C. Lee, M. M. Bell, F. D. Marks Jr., P. P. Dodge, and G. M. Barnes, 2011: Intercomparison of Ground-Based Velocity Track Display (GBVTD)-retrieved circulation centers and structures of Hurricane Danny (1997) from two coastal WSR-88Ds. *Mon. Wea. Rev.*, **139**, 153–174, https://doi.org/10.1175/2010MWR3036.1.

Musgrave, K. D., C. A. Davis, and M. T. Montgomery, 2008: Numerical simulations of the formation of Hurricane Gabrielle (2001). *Mon. Wea. Rev.*, **136**, 3151–3167, https://doi.org/10.1175/2007MWR2110.1.

Nguyen, L. T., and J. Molinari, 2012: Rapid intensification of a sheared, fast-moving hurricane over the Gulf Stream. *Mon. Wea. Rev.*, **140**, 3361–3378, https://doi.org/10.1175/MWR-D-11-00293.1.

——, and ——, 2015: Simulation of the downshear reformation of a tropical cyclone. *J. Atmos. Sci.*, **72**, 4529–4551, https://doi.org/10.1175/JAS-D-15-0036.1.

Nolan, D. S., and L. D. Grasso, 2003: Nonhydrostatic, three-dimensional perturbations to balanced, hurricane-like vortices.

Part II: Symmetric response and nonlinear simulations. *J. Atmos. Sci.*, **60**, 2717–2745, https://doi.org/10.1175/1520-0469(2003)060<2717:NTPTBH>2.0.CO;2.

——, Y. Moon, and D. P. Stern, 2007: Tropical cyclone intensification from asymmetric convection: Energetics and efficiency. *J. Atmos. Sci.*, **64**, 3377–3405, https://doi.org/10.1175/JAS3988.1.

Paterson, L. A., B. N. Hanstrum, N. E. Davidson, and H. C. Weber, 2005: Influence of environmental vertical wind shear on the intensity of hurricane-strength tropical cyclones in the Australian region. *Mon. Wea. Rev.*, **133**, 3644–3660, https://doi.org/10.1175/MWR3041.1.

Peirano, C. M., K. L. Corbosiero, and B. H. Tang, 2016: Revisiting trough interactions and tropical cyclone intensity change. *Geophys. Res. Lett.*, **43**, 5509–5515, https://doi.org/10.1002/2016GL069040.

Pendergrass, A. G., and H. E. Willoughby, 2009: Diabatically induced secondary flows in tropical cyclones. Part I: Quasi-steady forcing. *Mon. Wea. Rev.*, **137**, 805–821, https://doi.org/10.1175/2008MWR2657.1.

Reasor, P. D., and M. T. Montgomery, 2001: Three-dimensional alignment and corotation of weak, TC-like vortices via linear vortex Rossby waves. *J. Atmos. Sci.*, **58**, 2306–2330, https://doi.org/10.1175/1520-0469(2001)058<2306:TDAACO>2.0.CO;2.

——, and M. D. Eastin, 2012: Rapidly intensifying Hurricane Guillermo (1997). Part II: Resilience in shear. *Mon. Wea. Rev.*, **140**, 425–444, https://doi.org/10.1175/MWR-D-11-00080.1.

——, and M. T. Montgomery, 2015: Evaluation of a heuristic model for tropical cyclone resilience. *J. Atmos. Sci.*, **72**, 1765–1782, https://doi.org/10.1175/JAS-D-14-0318.1.

——, ——, and L. D. Grasso, 2004: A new look at the problem of tropical cyclones in vertical shear flow: Vortex resiliency. *J. Atmos. Sci.*, **61**, 3–22, https://doi.org/10.1175/1520-0469(2004)061<0003:ANLATP>2.0.CO;2.

——, M. D. Eastin, and J. F. Gamache, 2009: Rapidly intensifying Hurricane Guillermo (1997). Part I: Low-wavenumber structure and evolution. *Mon. Wea. Rev.*, **137**, 603–631, https://doi.org/10.1175/2008MWR2487.1.

——, R. Rogers, and S. Lorsolo, 2013: Environmental flow impacts on tropical cyclone structure diagnosed from airborne Doppler radar composites. *Mon. Wea. Rev.*, **141**, 2949–2969, https://doi.org/10.1175/MWR-D-12-00334.1.

Riemer, M., M. T. Montgomery, and M. E. Nicholls, 2010: A new paradigm for intensity modification of tropical cyclones: Thermodynamic impact of vertical wind shear on the inflow layer. *Atmos. Chem. Phys.*, **10**, 3163–3188, https://doi.org/10.5194/acp-10-3163-2010.

——, ——, and ——, 2013: Further examination of the thermodynamic modification of the inflow layer of tropical cyclones by vertical wind shear. *Atmos. Chem. Phys.*, **13**, 327–346, https://doi.org/10.5194/acp-13-327-2013.

Rios-Berrios, R., and R. D. Torn, 2017: Climatological analysis of tropical cyclone intensity changes under moderate vertical wind shear. *Mon. Wea. Rev.*, **145**, 1717–1738, https://doi.org/10.1175/MWR-D-16-0350.1.

Rogers, R. F., S. S. Chen, J. Tenerelli, and H. E. Willoughby, 2003: A numerical study of the impact of vertical shear on the distribution of rainfall in Hurricane Bonnie (1998). *Mon. Wea. Rev.*, **131**, 1577–1599, https://doi.org/10.1175//2546.1.

——, P. Reasor, and S. Lorsolo, 2013: Airborne Doppler observations of the inner-core structural differences between intensifying and steady-state tropical cyclones. *Mon. Wea. Rev.*, **141**, 2970–2991, https://doi.org/10.1175/MWR-D-12-00357.1.

——, ——, and J. Zhang, 2015: Multiscale structure and evolution of Hurricane Earl (2010) during rapid intensification. *Mon. Wea. Rev.*, **143**, 536–562, https://doi.org/10.1175/MWR-D-14-00175.1.

——, J. Zhang, J. Zawislak, H. Jiang, G. Alvey, E. Zipser, and S. Stevenson, 2016: Observations of the structure and evolution of Hurricane Edouard (2014) during intensity change. Part II: Kinematic structure and the distribution of deep convection. *Mon. Wea. Rev.*, **144**, 3355–3376, https://doi.org/10.1175/MWR-D-16-0017.1.

Schecter, D. A., and M. T. Montgomery, 2003: On the symmetrization rate of an intense geophysical vortex. *Dyn. Atmos. Oceans*, **37**, 55–88, https://doi.org/10.1016/S0377-0265(03)00015-0.

——, ——, and P. D. Reasor, 2002: A theory for the vertical alignment of a quasigeostrophic vortex. *J. Atmos. Sci.*, **59**, 150–168, https://doi.org/10.1175/1520-0469(2002)059<0150:ATFTVA>2.0.CO;2.

Shapiro, L., and H. E. Willoughby, 1982: The response of balanced hurricanes to local sources of heat and momentum. *J. Atmos. Sci.*, **39**, 378–394, https://doi.org/10.1175/1520-0469(1982)039<0378:TROBHT>2.0.CO;2.

Shimada, U., M. Sawada, and H. Yamada, 2016: Evaluation of the accuracy and utility of tropical cyclone intensity estimation using single ground-based Doppler radar observations. *Mon. Wea. Rev.*, **144**, 1823–1840, https://doi.org/10.1175/MWR-D-15-0254.1.

——, ——, and ——, 2018: Doppler radar analysis of the rapid intensification of Typhoon Goni (2015) after eyewall replacement. *J. Atmos. Sci.*, **75**, 143–162, https://doi.org/10.1175/JAS-D-17-0042.1.

Smith, R. K., and M. T. Montgomery, 2016: The efficiency of diabatic heating and tropical cyclone intensification. *Quart. J. Roy. Meteor. Soc.*, **142**, 2081–2086, https://doi.org/10.1002/qj.2804.

——, ——, and V. S. Nguyen, 2009: Tropical cyclone spin-up revisited. *Quart. J. Roy. Meteor. Soc.*, **135**, 1321–1335, https://doi.org/10.1002/qj.428.

Stevenson, S. N., K. L. Corbosiero, and J. Molinari, 2014: The convective evolution and rapid intensification of Hurricane Earl (2010). *Mon. Wea. Rev.*, **142**, 4364–4380, https://doi.org/10.1175/MWR-D-14-00078.1.

Susca-Lopata, G., J. Zawislak, E. J. Zipser, and R. F. Rogers, 2015: The role of observed environmental conditions and precipitation evolution in the rapid intensification of Hurricane Earl (2010). *Mon. Wea. Rev.*, **143**, 2207–2223, https://doi.org/10.1175/MWR-D-14-00283.1.

Tang, B., and K. A. Emanuel, 2010: Midlevel ventilation's constraint on tropical cyclone intensity. *J. Atmos. Sci.*, **67**, 1817–1830, https://doi.org/10.1175/2010JAS3318.1.

Ueno, M., 2007: Observational analysis and numerical evaluation of the effects of vertical wind shear on the rainfall asymmetry in the typhoon inner-core region. *J. Meteor. Soc. Japan*, **85**, 115–136, https://doi.org/10.2151/jmsj.85.115.

——, 2008: Effects of ambient vertical wind shear on the inner-core asymmetries and vertical tilt of a simulated tropical cyclone. *J. Meteor. Soc. Japan*, **86**, 531–555, https://doi.org/10.2151/jmsj.86.531.

Wang, Y., and G. J. Holland, 1996: The beta drift of baroclinic vortices. Part I: Adiabatic vortices. *J. Atmos. Sci.*, **53**, 411–427, https://doi.org/10.1175/1520-0469(1996)053<0411:TBDOBV>2.0.CO;2.

——, Y. Rao, Z.-M. Tan, and D. Schnemann, 2015: A statistical analysis of the effects of vertical wind shear on tropical cyclone intensity change over the western North Pacific. *Mon. Wea. Rev.*, **143**, 3434–3453, https://doi.org/10.1175/MWR-D-15-0049.1.

Wu, L., S. A. Braun, J. Halverson, and G. Heymsfield, 2006: A numerical study of Hurricane Erin (2001). Part I: Model verification and storm evolution. *J. Atmos. Sci.*, **63**, 65–86, https://doi.org/10.1175/JAS3597.1.

Zhao, K., M. Xue, and W.-C. Lee, 2012: Assimilation of GBVTD-retrieved winds from single-Doppler radar for short-term forecasting of super typhoon Saomai (0608) at landfall. *Quart. J. Roy. Meteor. Soc.*, **138**, 1055–1071, https://doi.org/10.1002/qj.975.

Zhu, T., D.-L. Zhang, and F. Weng, 2004: Numerical simulation of Hurricane Bonnie (1998). Part I: Eyewall evolution and intensity changes. *Mon. Wea. Rev.*, **132**, 225–241, https://doi.org/10.1175/1520-0493(2004)132<0225:NSOHBP>2.0.CO;2.